

Dimensionless pedestal identity plasmas on Alcator C-Mod and JET

G P Maddison¹, A E Hubbard², J W Hughes², J A Snipes^{2‡},
B LaBombard², I M Nunes³, M N A Beurskens¹, S K Erents¹,
M A H Kempenaars¹, B Alper¹, S D Pinches¹, M Valovič¹,
R Pasqualotto⁴, A Alfier⁴, E Giovannozzi⁵
and JET EFDA contributors^{*}

¹ EURATOM/UKAEA Fusion Association, Culham Science Centre,
Abingdon, Oxon. OX14 3DB, UK.

² Plasma Science and Fusion Centre, Massachusetts Institute of
Technology, 175 Albany Street, Cambridge, MA 02139, USA.

³ IPFN, Associação EURATOM-IST, 1096 Lisbon, Portugal.

⁴ Consorzio RFX, EURATOM-ENEA Association, Padova, Italy.

⁵ Associazione EURATOM-ENEA, ENEA Centro Ricerche Frascati,
Italy.

[‡] current address: ITER Organization, Cadarache, 13108 St. Paul-lez-Durance, France.

^{*} see appendix of F Romanelli *et al.*, Fusion Energy (Proceedings 22nd International Conference, Geneva, 2008) IAEA.

Abstract

Experiments on the Alcator C-Mod and JET tokamaks with identical values of non-dimensional variables at the pedestal top are expected to have the same local plasma transport for a ratio > 4 in absolute size and thus can help to clarify other effects in pedestal formation. At the high and low fields (7.9 T, 1.4 T respectively) involved, natural-density H-modes on C-Mod were of conventional ELM-free type, while those on JET were steady but with only small, sporadic ELMs. Nevertheless, they remained close to a common regime and a good non-dimensional match at the edge was achieved for highest C-Mod densities spanned. Pedestal profiles were measured with a fine-resolution edge Thomson scattering diagnostic on C-Mod, plus a new high-resolution (HRTS) system on JET. Electron temperature widths on JET were estimated to lie between scaled C-Mod levels and somewhat broader fitted shapes. Density pedestal widths, however, were reliably found to be proportionally broader than on C-Mod, signalling an influence other than plasma transport in their formation. Edge particle sources were modelled for both devices with the 1-D kinetic KN1D code and corroborated for JET using the 2-D fluid-plasma / kinetic-gas EDGE2D-NIMBUS suite. Overlaying normalised profiles of ionisation rates suggested density pedestal thicknesses were at least partly related to neutral-particle penetration. Such dependence implies their scaling is not Kadomtsev-like for the collisional, low-normalised-pressure conditions investigated, so precluding unambiguous scans versus dimensionless variables like normalised Larmor radius.

1. Introduction

During its inductive phase of operation, the ITER next-step tokamak plans to reach a power amplification ratio of $Q = 10$ using a plasma regime based upon the steady-state ELMy H-mode^[1]. This regime is characterised by high energy confinement due in large part to a narrow region of reduced transport, or “barrier”, at the edge, over which steeper gradients of plasma properties are sustained. An edge “pedestal” is formed, topped by higher values than would be achieved with smoother L-mode profiles^[2,3,4]. Such conditions are particularly advantageous since they enclose the greatest possible volume of elevated properties, and a clear correlation between total and pedestal (ie $3/2 \times$ pedestal pressure \times plasma volume) stored energies is found for H-modes in several existing experiments^[5-11]. In this sense the pedestal provides a crucial boundary condition for core performance, at least under conventional gas fuelling^[12]. Its formation and structure are therefore being carefully studied, concentrating particularly upon scalings of its heights n^{ped} , T^{ped} , p^{ped} and widths Δ_n , Δ_T , Δ_p in density, temperature and pressure respectively, for both electron and ion channels. At the present time, these dependencies are not yet fully resolved^[2,3,4], there being even conflicting results eg with respect to apparent correlation of widths with poloidal Larmor radii of edge ions^[5,13,14], or lack of it^[4,15].

Formation of the density pedestal differs fundamentally from that in temperature since its primary sources, viz ionisation of recycled and puffed particles, enter from the plasma boundary and tend to be concentrated in the edge itself. The implied steady-state local balance :-

$$\nabla \cdot \Gamma_i = S_i \quad , \quad (1)$$

where $\Gamma_i \text{ m}^{-2} \cdot \text{s}^{-1}$ is ion flux density and $S_i \text{ m}^{-3} \cdot \text{s}^{-1}$ ionisation rate, is independent of confinement regime and so applies to both L and H cases. A 1-D approximation of general edge density profiles was originally elaborated from (1) by Wagner and Lackner^[16], developing a previous treatment by Engelhardt^[17,18]. More recently, this description has been revisited by Mahdavi^[19,20] to incorporate changes in poloidal flux expansion $E(\theta)$ which in 2-D may affect main source input relative to profile data. The resulting electron density inside the separatrix, in an assumed pure plasma, may be written :-

$$n_e = n_e^{\text{ped}} \tanh\left(\frac{x}{\tilde{\lambda}_0} + C\right) \quad ; \quad (x \geq 0) \quad , \quad (2)$$

$$C = \frac{1}{2} \sinh^{-1}\left(\frac{2D_{\perp}}{\tilde{\lambda}_0} \sqrt{\frac{\tau_{\parallel}^{\text{SOL}}}{D_{\perp}^{\text{SOL}}}}\right) \quad ,$$

where coordinate $x = 0$ at the separatrix and increases towards the magnetic axis, D_{\perp} , D_{\perp}^{SOL} $\text{m}^2 \cdot \text{s}^{-1}$ are particle diffusivities for $x > 0$, $x < 0$ (the scrape-off layer) respectively, each supposed constant, and $\tau_{\parallel}^{\text{SOL}}$ is a mean residence time of ions in the latter (\sim connection length over sound speed). Length $\tilde{\lambda}_0 \equiv (2/E^*)\lambda_0^{\text{ped}} = (2/E^*)v_{0,x}/(n_e^{\text{ped}}\varsigma_{\text{I}})$ is an effective mean-free path for impinging atoms, taken to have speed $v_{0,x}$ and ionisation rate coefficient $\varsigma_{\text{I}} \text{ m}^3 \cdot \text{s}^{-1}$, both assumed constant, while $E^* \equiv (1/E) \int n_0|_{\text{sep}} E d\theta / \int n_0|_{\text{sep}} d\theta$ is weighted with possibly non-uniform atom density n_0 around the separatrix. Expression (2) reveals that peripheral density tends to adopt a pedestal-like shape with width determined by penetration

of neutral particles, as invoked in some L to H transition models^[21]. Moreover it depends only mildly upon transport (D_{\perp}) through the boundary condition C , such that the profile is not qualitatively changed if a barrier in particle diffusion is also incorporated within its breadth^[22]. In fact, it remains unclear whether an edge barrier in particle, as opposed to thermal (χ_{\perp}), transport necessarily accompanies the transition into H-mode^[20,22,23], although reductions in coincident density fluctuations are commonly seen^[24-27]. Up to the weak contribution through C , (2) indicates a width $\Delta_{n_e} \sim 2\tilde{\lambda}_0 \propto 1/n_e^{\text{ped}}$, so the density profile becomes narrower and steeper as it increases in height owing to growing opacity to incident atoms. This signature of a fuelling-dominated pedestal has indeed been observed over a range of plasma states in the DIII-D^[3,20,28-30], and for H-modes also MAST^[31], tokamaks. However, it is absent from H-modes spanning rising n_e^{ped} on ASDEX Upgrade^[32], where Δ_{n_e} remains almost constant, as well as Alcator C-Mod^[4,10,33,34], for which Δ_{n_e} again varies little or is apt even to increase with n_e^{ped} . Evidently another mechanism, namely plasma transport, can therefore compete with sources in producing the density pedestal, and the question naturally arises for what conditions each influence might predominate, or be in balance. Furthermore, since edge pressure gradient is typically limited by MHD-like constraints^[2,4,23,33-39] (although second-stability against ideal-ballooning modes is often seen on DIII-D^[2,15,40,41]), density structure could potentially affect that in temperature too $1/\Delta_{T_e} \sim |\nabla p|/(2n_e^{\text{ped}}T_e^{\text{ped}}) - 1/\Delta_{n_e}$.

Neutral-particle and edge plasma properties tend to be linked through recycling and can be difficult to alter independently in a single machine. The governing equations of magnetised toroidal plasmas can however be cast in terms of key dimensionless variables: normalised collisionality ν_{*e} ; Larmor radius ρ_* ; pressure β ; plus magnetic configuration parameters, so that for fixed values of these numbers, their behaviour is in principle fixed^[42-45]. Realising the same edge ν_{*e}^{ped} , ρ_*^{ped} , β^{ped} in a given equilibrium shape on different machines should therefore preserve local transport and help to emphasize effects of distinct features like recycling sources, which do not a priori follow equivalent inter-machine scalings^[44,45]. It should be noted, though, that other operational conditions, such as proximity to the Greenwald density limit^[46] or margin over H-mode power threshold^[47,48], also do not conform to the scalings and hence could themselves affect comparisons between devices. Nevertheless the technique of dimensionless pedestal identity between tokamaks can potentially clarify underlying contributions to profiles and has been pursued in a number of pairwise studies^[23,49-51]. Here new results are reported between Alcator C-Mod and JET, which provide a particularly stringent test since they span more than a factor of 4 in absolute size and differ markedly in recycling regime. Thus, for example, matching edge profiles for strongly contrasting source distributions would suggest dominance of plasma processes within the pedestal, while clear departures for non-dimensionally identical properties at their tops could signify the opposite. Ideally, scans through $\nu_{*e}^{\text{ped}}, \rho_*^{\text{ped}}, \beta^{\text{ped}}$ space would be performed to seek possible borders between these different eventualities. In the next section, the method of dimensionless pedestal identity as applied between C-Mod and JET is outlined. Note we draw a distinction explicitly between “identity”, where all essential variables are duplicated simultaneously so plasma effects are in principle reproduced, and “similarity”, where typically all but one variable are copied to expose dependence upon the latter as just it is incremented. Then global features of respective H-modes achieving closely identical pedestal tops are compared, with a view particularly towards resilience of core properties. For C-Mod, these plasmas comprise some of its scarcer cases at almost 8 T. This leads into a

detailed examination of edge profiles, using a recognised form of parameterisation unambiguously to extract their heights, widths etc^[4,10,33]. On JET, its new high-resolution Thomson scattering (HRTS) diagnostic^[52,53] has been exploited to obtain data below the dynamic range of most of its other systems. Such a facility allows a crucial advance on previous C-Mod identity attempts on JET, for which no unequivocal pedestal values could be obtained^[54,55]. To ascertain whether contrasting fuelling sources may be playing a role especially in density pedestal formation requires modelling of neutral-particle influxes, and a 1-D kinetic treatment^[33,54,56] calibrated by measurements of torus gas pressures is thereafter applied to conditions in each machine. Again for JET, this is corroborated by 2-D calculations using a coupled fluid-plasma / kinetic-neutral-particle code suite, the EDGE2D-NIMBUS model^[57,58]. Finally, a summary is given and implications of our results regarding pedestal scalings are briefly considered.

2. Non-dimensional scalings between devices

To preserve local plasma behaviour, the essential dimensionless variables^[59] :-

$$\begin{aligned} v_{*e} &\propto Z_{\text{eff}} \frac{q_{95}}{\varepsilon^{5/2}} a \frac{n_e}{T_e^2} \quad , & \rho_* &\propto \frac{\sqrt{T_e}}{a B_0} \quad , \\ \beta &\propto \frac{n_e T_e}{B_0^2} \quad , & q_{95} &\propto \varepsilon \frac{a B_0}{I_p} \quad , \end{aligned} \quad (3)$$

where $\varepsilon \equiv a/R_0$ is inverse aspect ratio, Z_{eff} effective ionic charge and q_{95} edge safety factor, should keep identical values at least at the pedestal top^[4,23,50]; the extent to which matching profiles are realised over the whole pedestal region then measures their control by plasma processes. Constancy of (3) between two tokamaks with minor radii $a_{[1]}, a_{[2]}$ implies main operational factors field B_0 , current I_p , fuelling and heating must be adjusted so respective dimensional parameters fulfill the ratios^[4,23,49,50] :-

$$\begin{aligned} \frac{B_{0[1]}}{B_{0[2]}} &= \left(\frac{a_{[2]}}{a_{[1]}} \right)^{5/4} \quad , & \frac{I_{p[1]}}{I_{p[2]}} &= \left(\frac{a_{[2]}}{a_{[1]}} \right)^{1/4} \quad , \\ \frac{n_{e[1]}^{\text{ped}}}{n_{e[2]}^{\text{ped}}} &= \left(\frac{a_{[2]}}{a_{[1]}} \right)^2 \quad , & \frac{T_{e[1]}^{\text{ped}}}{T_{e[2]}^{\text{ped}}} &= \sqrt{\frac{a_{[2]}}{a_{[1]}}} \quad . \end{aligned} \quad (4)$$

Note this assumes majority species plus all other details of the magnetic configuration are unchanged in each device, as explained below. Similar consideration of energy fluxes and eg cyclotron periods elapsed leads to equivalent scalings of approximate input power and time passed in the two participants^[50] :-

$$P \sim a^2 n_e T_e^{3/2} \quad \Rightarrow \quad \frac{P_{[1]}}{P_{[2]}} \sim \left(\frac{a_{[2]}}{a_{[1]}} \right)^{3/4} \quad , \quad (5)$$

$$\tau = \int_{t_A}^{t_B} \omega_{ce} dt' \quad \Rightarrow \quad \frac{(t_B - t_A)_{[1]}}{(t_B - t_A)_{[2]}} \approx \left(\frac{a_{[1]}}{a_{[2]}} \right)^{5/4} \quad . \quad (6)$$

This last approximation usefully allows counterpart signals, appropriately synchronised, to be overlaid on a common time axis. Thus, over intervals where quantities are non-dimensionally matched, for instance $n_{e[1]}^{\text{ped}}(t_{[1]}) a_{[1]}^2(t_{[1]}) \approx n_{e[2]}^{\text{ped}}(\{a_{[1]}/a_{[2]}\}^{5/4} t_{[2]}) a_{[2]}^2(\{a_{[1]}/a_{[2]}\}^{5/4} t_{[2]})$, the size ratio in curly brackets being an average during the period of interest.

Applying these relations to pairing of Alcator C-Mod and JET, for which $a_{\text{JET}}/a_{\text{C-Mod}} \approx 4.1$, implies the guide-line respective pulse parameters outlined in Table 1. Here quantities have been chosen according to available power and edge ranges expected to favour H-mode regime in C-Mod, based upon existing experience^[4,10,60,61]. Note input power and pedestal temperature are of course not independent, the former being estimated only for guidance. A notable feature is the capacity of C-Mod to work at very high field, almost 8 T, which considerably ameliorates the counterpart value ($\approx 6 \times$ smaller) required on JET compared with earlier edge identity attempts^[54,55]. Nevertheless its specified field of 1.4 T remains below normal ranges and for example excludes some standard diagnostics such as ECE radiometry, for which conditions are consistently above the associated cut-off density ($\approx 1.1 \times 10^{19} \text{ m}^{-3}$ at $R = 3.8 \text{ m}$).

A reference series of deuterium plasmas at the requisite field and current on C-Mod was obtained by applying maximum available ion cyclotron resonance heating (ICRH) at 80 MHz, exploiting ^3He -minority second-harmonic absorption, which at 7.9 T yields resonance almost exactly on axis. Density during its typical H-modes is very insensitive to gas fuelling^[34], so plasma states at the unfuelled, “natural” density^[62] were scanned by varying their Ohmic “target” level $n_{e\Omega}$ prior to imposing ICRH. This latter quantity can actually exert an important influence on their succeeding H-mode properties. In particular there tends to be a threshold value dividing (in combination with q_{95} and magnetic shaping parameters) principal types observed on C-Mod^[4,10,39,63,64], namely into standard ELM-free H-regime at lower $n_{e\Omega}$ and stationary, ELM-free “enhanced $D\alpha$ ” (EDA) H-regime at higher $n_{e\Omega}$. Further characteristics of these alternative confinement modes are considered below. Matching plasmas at the scaled field and current on JET were then sought by a fine power scan, again always at the “natural” density, in turn using ^1H -minority second-harmonic ICRH at 42 MHz, which similarly gives near-axial absorption. Comparability of the heating schemes in each device was pursued for greatest equivalence of their respective plasmas, although the extent to which core power-deposition profiles and electron-ion partition might affect edge properties remains uncertain^[50]. However, restriction just to RF additional heating ensured no direct momentum input in both cases, favouring least difference between their toroidal-rotation velocities (not directly measured).

Table 1. Design parameters for H-mode pedestal identity between Alcator C-Mod and JET (shown [grey], actual values realised in a closely matching shot pair; see Fig.2 and text for detailed discussion).

quantity	C-Mod	JET	size scaling
B_0 (T)	7.9 [7.9]	1.4 [1.4]	$a^{-5/4}$
I_p (MA)	1.3 [1.3]	0.91 [0.91]	$a^{-1/4}$
P (MW)	3.7 [3.2]	1.3 [3.0]	$a^{-3/4}$
n_e^{ped} (10^{19} m^{-3})	20. [30.]	1.2 [1.8]	a^{-2}
T_e^{ped} (eV)	550. [500.]	270. [250.]	$a^{-1/2}$

Precisely reproducing plasma behaviour also relies upon forming the same magnetic shape in each machine, so that balances of transport components and stability properties remain unchanged. In particular, inverse aspect ratio ϵ has been taken to be constant in deriving (4), in contrast to some other studies^[23,51,65]. A common single-null diverted configuration was chosen for C-Mod and JET, embodying elongation and triangularity as high as jointly achievable to help promote H-modes with smaller ELM fluctuations^[6,66-69]. Repetition of this equilibrium on each machine is illustrated in Fig.1, where key parameters determined where appropriate from EFIT reconstructions are overlaid, scaling the time-axis of JET quantities to that of C-Mod as described above. Dimensional signals, field and current, are also scaled with minor radius in accordance with (4). An excellent match within the comparison interval (vertical dotted lines) was clearly obtained, except for small discrepancies in ϵ and lower triangularity δ^1 ($\approx 6\%$, $\approx 7\%$ respectively). Superimposition of the scaled separatrices also suggests a departure in the next-order moment of squareness. Note $q_{95} \approx 4.2$, a moderately high value found to promote EDA H-mode on C-Mod, at least for lower field^[4,10,39,63,64]. More striking in Fig.1, though, is the large difference in renormalised pressure^[70] $\beta_N \equiv [\beta_t \text{ \%}] [a \text{ m}] [B_t \text{ T}] / [I_p \text{ MA}]$, also plotted. This contrast in global behaviour typified the two sets of plasmas gathered and signifies a significant difference in their core features even when their edges were well matched.

3. Global plasma properties and fluctuations

Detailed examination of pedestal profiles is elaborated in the next section, but first certain global aspects of respective shots are considered, to help place them in the context of H-modes generally prevailing on each device and crucially to substantiate physical comparability of their edge regimes. Basic properties of a shot pair coming closest to dimensionless identity are summarised in Fig.2. As before, time-scales of JET signals are scaled with the ratio of minor radii to allow them to be overlaid on C-Mod ones, while dimensional quantities (powers, line-average density) are themselves scaled according to (5), (4), such that for accurate matching, counterpart traces would be expected to coincide. Shot #1060509011 demonstrates the plasma regime observed in all current C-Mod cases at 7.9 T: following transition into H-mode at ≈ 0.96 s, a clear ELM-free phase ensued, with conventional, monotonic increases in density and radiation owing to very high particle confinement^[39,60,63]. This was interrupted in #1060509011 at ≈ 1.1 s as radiation approached 100% of ICRH power (or potentially more, depending upon absorption efficiency), when a short burst of instabilities or back-transition into L-mode released some majority and/or impurity density, re-establishing a second ELM-free interval. Finally reversion to L-mode occurred at ≈ 1.19 s as input power dropped. Such ELM-free H-mode states are as found previously at ≈ 8 T on C-Mod^[60,61], the absence of EDA regime being possibly related to either too low “target” density $n_{e\Omega}$, and/or insufficient margin over power threshold, or some other factor yet to be identified for high field. Note for the second possibility, close proximity to the transition power level is suggested by a short “dithering” phase evident in $D\alpha$ emission just after entering H-mode in Fig.2, also as seen before^[60].

Corresponding signals for JET shot #70697 indicate rather different global behaviour, however. Its divertor $D\alpha$ light shows a sustained, low-recycling state with only small, irregular ELMs (eg notice the interval $1.0 \text{ s} \leq \{a_{\text{C-Mod}} / a_{\text{JET}}\}^{5/4} t_{\text{JET}} \leq 1.1 \text{ s}$), which are actually undetectable from noise on total stored energy (not plotted) deduced with a fast diamagnetic loop sampling at 5 kHz. Nevertheless stored energy or normalised pressure β_t ,

radiated power and plasma density in both the core and edge remained remarkably constant. This type of steady H-mode is very unusual for JET^[27] but was characteristic of the current series, except for a single instance, mentioned later. Its special nature may be associated with the high fraction of power radiated, apparent in Fig.2. Tomographic reconstruction of 2-D emission from multiple bolometric lines-of-sight in Fig.3 illustrates that a large part of this loss occurred from the confined region inside the separatrix, so plasma effluxes at the edge were in fact considerably depleted. Line-average $Z_{\text{eff}} \approx 2.7$ from visible bremsstrahlung further supports the presence of appreciable impurity content, which though not spatially resolved may have been distributed across the plasma radius, sufficiently to produce stable core radiation sinks. Normalised traces of central ECE for C-Mod and SXR emission for JET in Fig.2 also reveal respective sawtooth oscillations retained different frequencies over and above scaling of the latter according to (6), pointing towards different current-density profiles in the core of each plasma. Hence the general confinement regimes realised in C-Mod and JET, even for non-dimensionally matching pedestal tops, seem to be rather distinct.

The large, steady radiation loss from JET is likely to account for scaled input power having been substantially higher than in C-Mod, as depicted in the top panel of Fig.2. An alternative measure more usefully governing pedestal identity therefore becomes power efflux through the edge^[4,10,50] $P_{\text{SOL}} = P_{\Omega} + \eta P_{\text{RF}} - \partial W / \partial t - P_{\text{rad}}^{\text{bulk}}$, where P_{Ω} , P_{RF} are respectively Ohmic and ICRH input powers, η is absorption efficiency of the latter, W total stored energy, and $P_{\text{rad}}^{\text{bulk}}$ radiation loss from the confined zone. Estimates of P_{SOL} are additionally given in Fig.2, assuming $\eta = 1$ in the absence of accurate ray-tracing calculations for the second-harmonic schemes employed. Loss $P_{\text{rad}}^{\text{bulk}}$ is taken from bolometry excluding the divertor^[50] in each machine, which will thus involve an error should any significant emission have arisen from their scrape-off layers outside the separatrix (cf Fig.3). Within substantial uncertainties affecting P_{SOL} values, though, the former treatment is still sufficient to imply power flows through the edge were indeed roughly equivalent in most closely matching C-Mod and JET shot pairs. Respective scaled line-average densities were also comparable, at least at the peaks of C-Mod ELM-free phases (recall identity conditions sought only require n_e to correspond at the pedestal top). The largest departure remained in core pressures as disclosed by normalised signals β_i , recalling the associated β_N disparity in Fig.1, and consistent with the proportionally higher heating power in JET.

Differing β values suggest plasma profiles were dissimilar in the core despite their identity at the pedestal top. Data across the full plasma radius are presented for the same shot pair in Fig.4, combining a number of Thomson-scattering diagnostics on each device at the selected comparison time: for C-Mod, spectrometer- and polychromator- based core instruments are added to a millimetre-resolution edge system, all sampling at 60 Hz^[71-73], while for JET, core LIDAR^[74,75] firing at 4 Hz is complemented with a new HRTS diagnostic^[52,53] so far offering ≈ 1.5 cm resolution over the edge at 20 Hz in a 0.5 s window. To improve statistical significance, data from each diagnostic on C-Mod are averaged over 3 consecutive time-slices during the ELM-free phase, whereas for JET they are averaged over the 0.5 s HRTS interval. The latter data are then scaled according to (4) onto an adjusted mid-plane radial coordinate $\{a_{\text{C-Mod}} / a_{\text{JET}}\} R_{\text{mid}}^{\text{JET}}$ and superimposed on C-Mod quantities by aligning respective separatrices determined by EFIT. A small relative shift of ≈ 4 cm incurred reflects the small discrepancy in ϵ , already mentioned. Closely-matching profiles would then again overlies one another, but it is manifest from the resulting plot that core properties were far removed from equivalence, even though pedestal tops were precisely reproduced. These experiments

therefore provide a specific example where the pedestal furnishes only a weak boundary condition for the core, which is contrary to the usual situation for H-modes^[5 - 11], referred to in the Introduction. It is also directly in contrast to findings of a previous pedestal-identity trial between C-Mod and DIII-D^[50]. In other words, occurrence of strong radiation inside the separatrix on JET is able to exclude any “resilience” of full profiles^[76,77]. Note this is distinct from so-called “stiffness” of electron temperature shapes due to critical gradient scale-lengths^[78 - 81], checking of which is excluded specifically by the divergence in core densities and hence in potential thresholds.

Also as remarked before, commonest H-modes on C-Mod can be categorised as ELM-free or EDA types, one key distinction between them being related to turbulence signatures accompanying each regime^[4,39,63,64]. The quasi-stationary EDA-mode is characterised by high energy, but persistently reduced impurity and edge-particle, confinement owing to a constant, quasi-coherent mode (QCM) of order 100 - 150 kHz and medium toroidal periodicity $n \approx -15$ to -20 , believed to be of resistive type and which, being localised in the pedestal region, is thought to mediate continuous relaxation of edge gradients^[39,64,82 - 85]. Hence associated transport suppresses the uncontrolled rise of core density and radiation of ELM-free regime^[4,10,60,61], while avoiding intermittent, concentrated effluxes caused by ELM instabilities^[68,86]. Power spectra of magnetic fluctuations detected around the comparison interval between foregoing C-Mod and JET pulses are illustrated in Fig.5, where time and frequency scales related to C-Mod through (6) have again been superimposed on the JET case. For C-Mod shot #1060509011, an extraneous RF beatwave arose between antennae at 80 MHz and 80.5 MHz, but above this frequency (ie 500 kHz) strong, broadband Alfvén eigenmodes (AEs)^[87 - 90] driven by non-thermal ions were excited during the long ELM-free periods. Simultaneously, no QCM was apparent over lower frequencies, but instead many coherent stripes (possibly separated by multiples of the plasma rotation frequency) indicated the presence of a number of sustained modes. Toroidal mode-numbers estimated from correlated magnetic signals are exemplified in Fig.6, their negative sign in particular implying rotation in the electron-diamagnetic-drift direction. This sense was found even for the AEs probably owing to a positive, rather than usual negative, gradient of fast-ion β at the mode peaks. However, for the lower-frequency bands it endorses their similarity to a class of resistive, edge MHD instabilities prevalent between ELMs on JET over usual ranges of field and current and designated, in recognition of their spectrum, “washboard” modes (WBM)s^[91,92]. The C-Mod plasmas are therefore further disclosed as classic ELM-free H-mode states.

Considering the JET magnetic fluctuations in Fig.5 plus associated mode-numbers in Fig.6, there were again two RF beatwaves just above 100 kHz, below which several narrow bands of strong, toroidicity-induced Alfvén eigenmodes (TAEs)^[87 - 90] rotated more conventionally in the ion-drift direction ($n > 0$). Pronounced steadiness of these disturbances underlined that of the plasma generally despite the smallness of its ELMs. Complementing the TAEs were also accurately repeated, complex bursts of fast-particle modes at higher frequencies, so-called triangularity-induced or non-circular Alfvén eigenmodes (NAEs)^[87,93], although it is likely they have been aliased down significantly in the spectrogram due to the sampling rate of 500 kHz set for the diagnostic. Nevertheless they chirped up and down in frequency precisely in synchrony with the “double” sawteeth evident in Fig.2. Most interesting, however, were the electron-drift-directed modes between 30 - 40 kHz, their frequencies again sweeping moderately up and down very regularly in time with sawteeth. These features were of higher toroidal order, $n \approx -6$ to -10 , were more clearly visible in Fourier spectra of interferometer signals passing through the edge rather than the centre, and in addition were

detected on 24.3, 29.1 GHz channels of an ordinary-polarisation reflectometer^[94], returning respectively from densities of $\approx 0.7, 1 \times 10^{19} \text{ m}^{-3}$. All the latter properties consequently suggest localisation in the plasma edge. Such modes are distinct from the multiple-harmonic structure of WBMs, but it remains unclear yet whether they might comprise an analogue of the QCM for JET conditions, although as seen in Fig.5 their scaled frequencies would be somewhat above its typical range for C-Mod^[39,64,82 - 84].

The tendency on JET to produce a steady H-mode despite marked diminution of ELMs, as in #70697, lapsed only in a single pulse during the present power scan. For this preceding shot #70696 at $\approx 7\%$ lower ICRF heating, repeated cycles of conventional ELM-free H-mode were instead obtained, each with monotonically rising density and radiation. As the latter approached 100% of P_{RF} , a burst of instabilities or back-transition to L-mode was provoked, lowering both quantities again and allowing the ELM-free phase to restart. Thus a state very close to that seen for C-Mod pulse #1060509011 in Fig.2 was recovered, but the cycle period of $\approx 0.6 \text{ s}$ on JET allowed many of them to be repeated within its longer pulse duration. The pattern of behaviour recalled that seen in earliest attempts to replicate C-Mod plasmas on JET at higher field and current too^[95]. Emergence of similar cycles can even be noticed for #70697 after $\{a_{\text{C-Mod}}/a_{\text{JET}}\}^{5/4} t_{\text{JET}} > 1.26 \text{ s}$ in Fig.2, $t_{\text{JET}} > 65.2 \text{ s}$ in Fig.5, implying its proximity to familiar ELM-free conditions, which evidently can be accessed for only very small changes in properties. This resemblance is further supported by almost identical magnetic fluctuations in #70696, where the same bands of NAEs and TAEs were preserved, along with continuous modes between 30 - 50 kHz during each ELM-free interval. These latter only became slightly broader-band and, rather than obviously tracking sawtooth oscillations, dropped in frequency through the ELM-free phases, possibly as diamagnetic rotation responded to the density ramps. An equivalent modification can again be identified for #70697 after $t_{\text{JET}} > 65.2 \text{ s}$ in Fig.5. Hence it can be concluded that while core properties were significantly different in current C-Mod and JET plasmas, and fluctuation characteristics were also somewhat unlike, they were respectively in, or on the threshold of, ELM-free regimes, so their crucial edge regions may still be meaningfully compared.

4. Interpolation of pedestal parameters

Between ELMs in conventional H-modes, a gradual temporal evolution of pedestal profiles is known to occur as gradients approach and intercept MHD stability boundaries^[35 - 38], then being reset to shallower values for the cycle to repeat. Another crucial question is the extent to which higher frequency fluctuations of the profiles may be superimposed upon this slower growth. This issue becomes especially pertinent for quasi-stationary states with no or only minor ELMs, such as EDA regime or the present radiative, steady JET cases, since these latter could then dominate the time variation of edge quantities. Determining the level of unsteadiness is generally complicated, however, by finite performance of edge diagnostics, so that any observed deviations cannot often be unambiguously distinguished from “statistical” ones representing the measurement uncertainties^[52,53]. On C-Mod in particular, though, edge Thomson scattering data are sufficiently well resolved for it to be evident that around half of the variance in detected profiles can be attributable to genuine, fast, physical fluctuations^[10,33,50,54]. A similar finding of physical oscillations in edge profiles on time-scales much shorter than inter-ELM periods has also been discerned on DIII-D^[15]. Recall that ELM frequencies and amplitudes themselves generally exhibit a statistical nature even in steady H-mode phases^[86,96,97]. When comparing profiles effectively measured

instantaneously by Thomson scattering on different tokamaks, therefore, such variations would imply an exact correspondence should not necessarily be expected even if the governing physics were completely identical^[50,54]. A more reliable check should be provided by comparing data averaged over time, to reduce the effect of random profile fluctuations, whilst simultaneously gaining in statistical significance. Consequently C-Mod pedestal profiles captured at 60 Hz with its edge TS system^[72,73] have been averaged over 3 consecutive time-slices in least unsteady H-phases, in terms of $\partial W/\partial t$, of each pulse. As already noted, their ELM-free character excludes proper stationarity, but monotonic changes of edge properties over these chosen 33 ms intervals were typically small, as exemplified in Fig.7. Similarly, JET profiles measured at 20 Hz with its new HRTS diagnostic^[52,53] have been averaged over its 0.5 s window in each plasma.

To compare pedestal parameters between different devices, it is useful to introduce a standard interpolation of profile data so that heights, widths, maximum gradients and positions can be inferred in a consistent way. The simplest approach would be to apply a bilinear fit^[5], but a more flexible treatment, motivated in part by the Wagner and Lackner approximation^[16-18] of edge density outlined in the Introduction, is to fit a hyperbolic tangent function modified to incorporate a non-zero baseline plus an extra linear slope inside the pedestal top^[4,10,33] :-

$$f(R) = b + \frac{h}{2} \left[\tanh\left(\frac{R_c - R}{d}\right) + 1 \right] + m[R_c - d - R]\Theta(R_c - d - R) \quad , \quad (7)$$

$$\Theta(x) = \begin{cases} 0, & x < 0 \Rightarrow R > R_c - d \\ 1, & x \geq 0 \Rightarrow R \leq R_c - d \end{cases} \quad ,$$

where R_c is the pedestal central position for width $\Delta \equiv 2d$, total height $b + h$ and inner slope $-m$, while R is major-radial coordinate. Steepest gradient of $-h/(2d)$ also occurs at $R = R_c$. This form has been extensively applied before on both C-Mod^[4,10,33,64] and DIII-D^[3,15,98], and is practically equivalent to a fully differentiable adaptation developed by the latter^[99], although it should be borne in mind there are small systematic differences between height parameters inferred with each one for any given data. In the case of JET HRTS measurements, allowance is also made for their spatial resolution of ≈ 1.5 cm, since this could be of similar order to actual pedestal length scales. Its effect is approximated by convolution with a top-hat instrument function $I_{t-h}(R) = [1/w]\Theta(R + w/2)\Theta(w/2 - R)$ appropriate for Thomson scattering^[52,53,97], where Θ is the Heaviside unit step defined in (7) and $w = 1.5$ cm, giving an adjusted model function :-

$$\mu(R) = \int_{-\infty}^{\infty} f(R')I_{t-h}(R'-R)dR' = b + \frac{h}{2} + \frac{hd}{2w} \ln\left(\frac{\cosh([R_c + w/2 - R]/d)}{\cosh([R_c - w/2 - R]/d)}\right) + \quad (8)$$

$$\begin{cases} m[R_c - d - R] & , & R \leq R_c - d - w/2 \\ \frac{m}{w} \left[\frac{[R_c - d]^2}{2} - \left[R - \frac{w}{2} \right] \left[R_c - d - \frac{R - w/2}{2} \right] \right] & , & R_c - d - w/2 \leq R \leq R_c - d + w/2 \\ 0 & , & R_c - d + w/2 \leq R \end{cases}$$

In other words, error-weighted, non-linear least-squares fitting of (7) is applied to averaged C-Mod edge TS profiles (cf Fig.7), resolved with millimetre precision, and of (8) to averaged JET HRTS data over the peripheral region $3.65 \text{ m} < R \leq 3.86 \text{ m}$, both instances being mapped onto mid-plane major radius using EFIT reconstructions.

Implementation of HRTS in JET has permitted measurements below the previous lower ranges of other diagnostic systems^[54,55], but outermost points still tend to reach its detection limits. An additional approximation has therefore been invoked to assist interpolation of profile shapes, exploiting the fact that in cases examined, no distinguishable signal occurred in any spectrometer channel of the line-of-sight at 3.86 m. From associated transmission functions, plasma values at this position may thus be estimated to be zero within some fraction of the nearest reliable density value ($\pm \text{few} \times 10^{18} \text{ m}^{-3}$) and roughly $\pm 10 \text{ eV}$. Such a fall-off is further supported by presence of a signal just in channel 1 of the line-of-sight at 3.84 m, implying a temperature there below 40 - 70 eV, but this is considered less certain and not included in fits. Pedestal parameters determined for JET are therefore derived on the basis of this particular model. An attendant qualification is that only a single HRTS datapoint tends to remain in the steep gradient region of temperature pedestals (cf Fig.10), so formally they cannot be distinguished from a perfect step of zero width $b + [h + m[R_c - R]]\Theta(R_c - R)$, convolved with $I_{t-h}(R)$. Values found with (8) hence may be regarded as more intuitive, or upper bounds on the temperature widths. It may be noted finally that differences between parameters evaluated with (8) and (7) were actually very small for the JET cases addressed, ie their average profiles were interpreted as wide enough for HRTS resolution not significantly to influence them.

Subject to these caveats, pedestal heights inferred through the scans in each device are summarised in Fig.8(a), with standard deviations from the respective fitting procedures. Up to 3 different time-points are analysed in each C-Mod pulse (each one being an average over 3 neighbouring edge TS instants), which are listed in chronological order. They can be seen firstly to comprise a progression to higher pedestal pressure, realised by rising density n_e^{ped} for more nearly constant temperature T_e^{ped} . This somewhat unusual sequence^[5,6] implies ELM-free H-modes were sustained over a wide interval in pedestal pressure at 7.9 T. Plasmas from the JET power scan, listed in order of rising P_{RF} , are superimposed by scaling their properties to C-Mod ranges according to (4), ie density is multiplied by the square and temperature by the square root of the ratio of minor radii. Note some T_e^{ped} uncertainties are undetermined. However, it can be seen that apart from possible differences in local Z_{eff} values, which as mentioned above were not spatially resolved, identical pedestal-top dimensionless variables in both machines were achieved at the upper end of the C-Mod density span. Their correspondence is sketched, ie without uncertainties, in Fig.9, where the definition of collisionality is from Sauter^[59] and normalised pressure is approximated by $\beta^{\text{ped}} \approx 2[2\mu_0 n_e^{\text{ped}} T_e^{\text{ped}} / B_0^2]$, in the absence of charge-exchange information for ion temperature. Best matches were found between respective C-Mod and JET shot pairs: #1060509011 at 1.14 - 1.18 s (filled blue triangle) and #70699 (open triangle); #1060509011 at 1.06 - 1.10 s (filled green triangle) and #70697 (open diamond), as employed in preceding discussion of equilibrium and global features. Identity conditions obtained were for moderately collisional and low normalised pressure edges, as expected from their high density and field in C-Mod instances. Recall that in absolute terms, JET values elicited were far below ($3 - 5 \times$ in density, $5 - 7 \times$ in temperature) pedestal heights in ELMy H-modes at its usual levels of field, current and power^[5,6,100].

Accompanying pedestal widths Δ_{n_e} , Δ_{T_e} are plotted in Fig.8(b), again scaling JET quantities onto C-Mod ones with the size ratio, $\Delta' = \{a_{\text{C-Mod}} / a_{\text{JET}}\} \Delta^{\text{JET}}$. Proportionally, thicknesses for

C-Mod plasmas varied much less than the change in pedestal pressure, reflecting the typical robustness generally found for the former on C-Mod^[4,10,33,61]. Within uncertainties, density and temperature widths were also roughly equal and fell within the same intervals of $\approx 4-6$ mm most often seen for both ELM-free and EDA H-modes at lower field^[4,10,33,61]. Counterpart temperature widths on JET, particularly for the two best-matching shot pairs listed above, tended to lie from a similar scaled range to somewhat broader profiles, although as already noted these interpolations might properly be taken as upper bounds on Δ_{T_e} . With greater certainty, however, density pedestal widths were systematically broader than the C-Mod references, implying that even for non-dimensionally identical plasmas at their respective tops, Δ_{n_e} on JET was wider than would have been expected if it varied directly in proportion to machine size. In other words, linear scaling of Δ_{n_e} , which would signify equivalent edge profiles consistent with dominance of plasma effects, was not observed. This is in contrast to an earlier comparison between C-Mod and DIII-D^[50], where conformity of the whole time-averaged profiles was found when their tops were non-dimensionally matched, but in agreement with a subsequent identity trial between DIII-D and JET^[23], where again density pedestal thicknesses did not scale just with the size ratio. Further consideration of these differing results is given in the Summary below. The disparity in profiles is most easily seen by overlaying those C-Mod and JET data with closest identity at the pedestal tops, the latter once more scaled according to (4), interpolated onto normalised poloidal flux coordinate $\hat{\psi} \equiv [\psi - \psi_0] / [\psi_{\text{sep}} - \psi_0]$ from EFIT, when their correspondence may be checked by inspection, Fig.10. In both shot pairs depicted, C-Mod and scaled JET pedestal heights are clearly in good agreement. Density and temperature positions are practically coincident on C-Mod, whereas the density pedestal tends to lie somewhat inboard of that in temperature on JET, particularly in the second example, Fig.10(b), for which a wider T_e fit is suggested. On the other hand, the plot also serves to emphasize that a steeper form like the accompanying C-Mod T_e shape could be described through the JET measurements with only slightly reduced confidence. Less ambiguously, JET density widths are plainly broader, ie pedestal gradients are shallower, than their C-Mod partners, which are finally shifted (broken lines) on the plots to bring them into best alignment with JET, in order to accentuate the relative departure. Such a change in Δ_{n_e} is therefore suggestive of an influence in its formation other than explicitly identical edge plasma transport, as deduced previously in some individual DIII-D^[3,20,28-30] and MAST experiments^[31], prompting examination of associated source distributions.

5. Modelling of pedestal sources

Earlier studies of ionisation sources in the edges of C-Mod plasmas indicated that kinetic effects, ie departures from drifting Maxwellian phase-space distributions for impinging neutral particles, tended often to be significant^[33,54]. A simplified kinetic treatment has consequently been pursued to compare pedestal sources in the present plasma-identity shot pairs using the Kinetic Neutral 1-D (KN1D) transport code^[56], which solves the coupled Boltzmann equations for steady-state molecular and atomic distribution functions. One spatial dimension (x) is considered, oriented along the minor radius, plus two velocity components (v_x, v_r), assuming rotational symmetry about the principal axis ($v_r^2 = v_y^2 + v_z^2$). Measured gas pressure at the vessel wall is used to define the influx onto a set plasma background specified with respect to a reduced geometry, consisting of core, scrape-off layer (SOL) and “limiter-shadow” regions, with 100% recycling as thermal molecules from the

latter being taken to close the particle balance. Ionising and dissociative reactions are taken into account, along with multiple generations of charge-exchange events and elastic collisions on both ions and neutral particles, as well optionally as self-collisions within the molecules and atoms themselves^[56], although these were not selected here. Resulting source profiles strictly are appropriate to a situation where wall recycling dominates the refuelling^[54], ie contributions from divertor neutralisation are neglected, but our attention is concentrated mainly upon the shape of source terms within the pedestal, which depends only weakly on the foregoing boundary conditions.

Ion source distributions computed for the non-dimensionally matching C-Mod and JET shot pair in Fig.10(a) are shown in Fig.11. Note these last figures are each drawn on their own scales, not adjusted to ranges of one device as in preceding plots; thus modified tanh representations of plasma profiles copied into KN1D (faint lines) reveal the absolute levels in each pulse. Pedestal top positions, defined where heights $b + h$ are reached, are also marked to assist subsequent identification of features inside their breadths. Projections through the SOL and into the limiter shadow are restricted to typical density decay-lengths^[4,10] for C-Mod or just low levels ($T_e \geq 5$ eV, $n_e \geq 10^{18} \text{ m}^{-3}$ for JET) otherwise, although again these approximations do not affect source structure within the pedestal significantly. In the absence of further information, $T_i = T_e$ is additionally assumed. Input torus gas pressures are estimated with a ratiometric ionisation gauge for C-Mod and a Penning gauge for JET, characteristically yielding values more than $100\times$ lower on the latter (~ 0.002 mtorr ≈ 0.3 mPa) than the former (~ 0.3 mtorr ≈ 40 mPa) for these plasmas. Such a large ratio is in accordance with the much higher plasma densities established in the C-Mod cases. Hence note that ionisation rates are similarly over $100\times$ higher for C-Mod in Fig.11 (right-hand scales). Components directly from molecular dissociative ionisations and from atoms, plus their sum ($S_i \text{ m}^{-3} \cdot \text{s}^{-1}$), are traced, demonstrating that on both machines, molecular terms tend to peak in the near-SOL, while atomic ionisations and the total reach maxima just inside the pedestal. Qualitatively similar results were found in earlier 1-D modelling of C-Mod and related plasmas scaled to the dimensions of DIII-D and JET^[33,54]. Here the key point is that within the density pedestal, S_i exhibits a substantially exponential decay with fall-off lengths $\ell_S \equiv |\nabla \ln S_i|^{-1} \approx 1.3$ mm, 1.3 cm for C-Mod and JET respectively.

For JET, an extra check has been undertaken by computing its sources separately with the 2-D EDGE2D-NIMBUS code suite^[57,58]. This uses an axisymmetric discretisation of the EFIT equilibrium, adapted to actual geometry of the divertor target-plates with non-orthogonal meshing^[58]. Although developed mainly to address the SOL and divertor regions of plasmas, the pedestal can also be encompassed by projecting the grid somewhat inboard of the separatrix. A set of Braginskii^[101] coupled fluid-plasma transport equations for multiple ion species, momentum, ion and electron energies are solved, accounting for classical drift terms driven by gradients of electric potential, pressure and magnetic-field structure^[102 - 104]. Primary impurity carbon, evolved from divertor and main-chamber tiles, has been included for pulse #70697, with surface interactions treated by the Eckstein model^[105]. Linkage to the linear Monte Carlo neutral-particle simulator NIMBUS^[58] in turn provides a kinetic calculation of recycling and refuelling behaviour, considering the principal molecular and atomic reactions as in KN1D, but not elastic collisions. An optimum interpretation of #70697 has been inferred by adjusting upstream boundary conditions at the core interface, together with plasma cross-field (anomalous) transport coefficients, until a good match was simultaneously obtained to averaged HRTS data in the pedestal and target-facing electron density and temperature measured with embedded Langmuir probes at the outboard side of the divertor. Inboard probe data, though roughly matched too, were of poorer quality. Note

this approach reduces plasma diffusivities effectively to fitting parameters, but as before the effect is unimportant for source profiles within the pedestal, which are chiefly of interest. In the final steady state, an envelope of neutral gas was found completely to surround the plasma between its edge and the vessel wall, akin to the implicit assumption of a 1-D representation. Ionisation sources inside the separatrix, determined in 2-D, have been superimposed upon KN1D results in Fig.11(b) both by taking a section through the mid-plane and by averaging poloidally around magnetic surfaces. Recognising the variety of model inputs, the apparent agreement on absolute magnitudes may be somewhat fortuitous, but the closeness of decay-lengths ℓ_S relates to physically similar neutral-particle penetration for equal plasma properties in both codes. Hence confidence in plausibility of the KN1D solutions is increased.

Relative penetration of neutral particles into either plasma may be compared by normalising total ionisation rates S_i by their respective maximum value and replotting versus $\hat{\psi}$, Fig.12. It is immediately obvious the distribution of ion sources extends much deeper inside the JET case. Also indicated are locations interpolated onto $\hat{\psi}$ of the tops of the steep gradient regions in each density and temperature pedestal, defined as $R_c - d$, where these are the parameters of modified tanh fits to edge profiles, as involved in the KN1D calculations. The latter markers serve firstly to re-emphasize near coincidence of density and temperature pedestal widths and positions for C-Mod, $\Delta_{n_e}^{C-Mod} \approx \Delta_{T_e}^{C-Mod}$, $R_{cn_e}^{C-Mod} \approx R_{cT_e}^{C-Mod}$, already described in Fig.10. Intuitively such a condition, together with concentration of sources in the outer part of the temperature pedestal, might be expected to prevail if plasma processes were substantially controlling formation of the edge barrier. Such a state is typically inferred for H-modes on C-Mod^[4,33]. On the other hand, Fig.12 reiterates that the density pedestal on JET is clearly broader than and somewhat inboard of the temperature gradient zone, $\Delta_{n_e}^{JET} > \Delta_{T_e}^{JET}$, $R_{cn_e}^{JET} < R_{cT_e}^{JET}$, while it is unequivocally wider than the C-Mod value scaled with machine size, $\Delta_{n_e}^{JET} > \{a_{JET}/a_{C-Mod}\}\Delta_{n_e}^{C-Mod}$, counter to its scaling with plasma processes between devices as explained above. A much greater fraction of neutral-particle ionisation penetrates inside the top of the JET temperature pedestal, consistent with the edge density profile being decoupled and broadened by intrusion of fuel atoms.

It is interesting to compare these kinetic analyses of neutral-particle infiltration with simple fluid approximations frequently invoked. A crude estimate of steady-state mean-free path^[50] is, for instance, given by the Lehnert formula^[106,107] for atoms of constant temperature T_0 and mean velocity $v_{0,x}$ entering a quasi-neutral plasma of equal mass ions and constant density and temperature :-

$$\lambda_{0L} = \frac{1}{n_e} \sqrt{\frac{T_0}{m_i \zeta_I [\zeta_I + \zeta_{CX}]}} \quad , \quad (9)$$

where ζ_I , $\zeta_{CX} \text{ m}^3 \cdot \text{s}^{-1}$ are respective rate coefficients for ionisation and charge-exchange events. An indicative figure from (9) may therefore be derived at the centre of the density pedestal (R_{cn_e}) using atomic data from Janev^[108], similar to those employed in KN1D. Considering the pedestal-top identity shot pair addressed in Figs.11 & 12, this actually gives $\lambda_{0L} \approx 1.0 - 1.4 \text{ mm}$ for C-Mod and $\lambda_{0L} \approx 1.7 - 2.4 \text{ cm}$ for JET supposing $T_0 = 1 - 2 \text{ eV}$, which is in the typical range of Franck-Condon products of dissociative excitations^[109,110]. Such a value of course neglects effective heating of atoms by charge-exchange (and elastic)

collisions, which in the two KN1D calculations instead leads to mean atom energies of $T_0^{\text{C-Mod}} \approx 66 \text{ eV}$, $T_0^{\text{JET}} \approx 35 \text{ eV}$ at $R_{c_{n_e}}$. Nevertheless it appears that in this instance, a minimal picture of edge sources based just upon molecular dissociations in the SOL, like that embodied in the Engelhardt-Wagner-Lackner model^[16-18] outlined in the Introduction, would yield scale-lengths ℓ_S in the pedestal within a factor of 2 of those from KN1D mentioned above. A further simplification of the former fluid treatment and its later adaptation by Mahdavi^[19,20], namely assumption of a constant diffusion coefficient D_\perp , may also be examined by combining Fick diffusion^[22] $\Gamma_i = -D_\perp \nabla n_i$ with (1), implying in 1-D for a pure plasma having an edge profile as in (7) :-

$$D_\perp = - \left[\frac{\partial n_i}{\partial x} \right]^{-1} \int_0^x S_i(x') dx' \quad , \quad (10)$$

$$\text{where} \quad \frac{\partial n_i}{\partial R} = - \frac{h}{2d} \text{sech}^2 \left(\frac{R_c - R}{d} \right) - m \Theta(R_c - d - R) \quad . \quad (11)$$

Integrating the KN1D sources in Fig.11 consequently yields ion cross-field diffusivities over the C-Mod and JET pedestals as sketched in Fig.13, where a new normalised coordinate has been constructed to focus attention specifically upon the gradient zone of the density pedestal. The foot of the latter, defined as $R_{c_{n_e}} + d_{n_e}$ in each device, is set as origin, and distances are normalised by respective widths $2d_{n_e}$. The very low magnitudes of D_\perp deduced over the pedestal are qualified by the 1-D analysis, but are close to levels found previously in C-Mod from integration of sources derived with the Johnson and Hinnoy collisional-radiative rate equations^[11] from actual experimental distributions of $D\alpha$ emission^[33]. Coefficients satisfying dimensionless identity should scale between the two devices according to $D_\perp \sim a \sqrt{T_e} \sim a^{3/4} \Rightarrow (D_{\perp[1]} / D_{\perp[2]}) = (a_{[1]} / a_{[2]})^{3/4}$, and the JET result has again been so adapted to C-Mod ranges, ie the C-Mod and scaled JET functions should overlay one another if fulfilling identity interrelation. In fact they differ by less than a factor of 2 at the pedestal top $[R - R_{c_{n_e}} - d_{n_e}] / [2d_{n_e}] = -1$ (and across the entire edge, even coinciding at the separatrixes), so that allowing for modelling uncertainties particle transport is approximately matched, as expected for non-dimensionally identical conditions. In particular, though, it is evident D_\perp in Fig.13 is far from constant, but falls rapidly from $\sim 1 \text{ m}^2 \cdot \text{s}^{-1}$ in the SOL to a well in the pedestal, again as seen before^[33]. Note such a shape is predisposed by the form of the derivative (11) if sources remain concentrated in the outer part of the pedestal. Thus ion transport adopted in the Engelhardt-Wagner-Lackner-Mahdavi fluid approach may often be rather a poor approximation for plasmas with relatively shallow ionisation of neutral particles.

Returning to the 1-D source profiles in Fig.11, their decay-lengths ℓ_S within the density pedestal can be noticed to be in almost direct proportion to accompanying widths Δ_{n_e} themselves, namely $\Delta_{n_e}^{\text{JET}} / \Delta_{n_e}^{\text{C-Mod}} \approx 8.5$ here, compared with $a_{\text{JET}} / a_{\text{C-Mod}} \approx 4.1$. This equivalence is made even clearer in Fig.14(a) by overlaying total ionisation functions S_i , normalised by their maximum values, on the same normalised coordinate $[R - R_{c_{n_e}} - d_{n_e}] / [2d_{n_e}]$ defined for Fig.13. A similar plot for the second identity shot pair in Fig.10(b) is given in Fig.14(b), and although the coincidence of normalised C-Mod and JET ionisation rates is less exact, they can still be seen each to have the same normalised fall-off

in the pedestal. Furthermore, the latter is practically the same as for the first shot pair in Fig.14(a), to which they are roughly equal in pedestal heights n_e^{ped} , T_e^{ped} (cf Fig.8(a)). Slightly larger differences between respective cases in Fig.14(b) are disclosed by test calculation with KN1D to be due to the broader temperature pedestal inferred for JET pulse #70699, which as observed before may only be an upper bound on its true thickness. Thus kinetic modelling of refuelling in each machine for plasmas with most closely matching dimensionless variables at their pedestal tops suggests :-

$$\frac{\ell_S^{\text{JET}}}{\Delta_{n_e}^{\text{JET}}} \approx \frac{\ell_S^{\text{C-Mod}}}{\Delta_{n_e}^{\text{C-Mod}}} \Rightarrow \frac{\Delta_{n_e}^{\text{JET}}}{\Delta_{n_e}^{\text{C-Mod}}} \approx \frac{\ell_S^{\text{JET}}}{\ell_S^{\text{C-Mod}}} \quad (12)$$

in the collisional, low-normalised-pressure edges concerned. In other words, JET n_e profiles are broader in Fig.8(b) than identity scaling would suggest because their ionisation distributions are broader. Near coincidence of density and temperature pedestal positions and widths in the C-Mod instances makes it difficult to distinguish whether plasma processes or particle sources are predominantly governing their density profiles, but correlation (12) means it cannot be ruled out that they are also at least partly determined by sources under the specific conditions examined. From (2), the Engelhardt-Wagner-Lackner-Mahdavi^[16-20] picture would imply :-

$$\frac{\Delta_{n_{\text{EWLM}}}^{\text{JET}}}{\Delta_{n_{\text{EWLM}}}^{\text{C-Mod}}} \approx \frac{\tilde{\lambda}_0^{\text{JET}}}{\tilde{\lambda}_0^{\text{C-Mod}}} = \frac{E^{*\text{C-Mod}}}{E^{*\text{JET}}} \frac{v_{0x}^{\text{JET}}}{v_{0x}^{\text{C-Mod}}} \frac{n_e^{\text{ped C-Mod}}}{n_e^{\text{ped JET}}} \frac{\zeta_I^{\text{C-Mod}}}{\zeta_I^{\text{JET}}} \approx 15 \frac{E^{*\text{C-Mod}}}{E^{*\text{JET}}} \quad , \quad (13)$$

where in the last expression $v_{0x}^{\text{JET}} = v_{0x}^{\text{C-Mod}}$ has been assumed, in combination with $n_e^{\text{ped C-Mod}} / n_e^{\text{ped JET}} \approx 17$ and^[108] $\zeta_I^{\text{C-Mod}} / \zeta_I^{\text{JET}} \approx 0.9$ at the tops of the best-matching pairs of pedestals in Fig.14. Hence only a moderate change in the source-geometry term $E^{*\text{C-Mod}} / E^{*\text{JET}} \approx 0.6$ would be required to bring even the simplified particle-balance treatment of density pedestal formation into agreement with the ratio of thicknesses observed, its strong approximations notwithstanding. Such relative variation of $E^{*\text{C-Mod}} / E^{*\text{JET}}$ moreover would tend to comply with recycling, as already alluded to above, generally being main-chamber dominated in C-Mod^[112-115], but divertor dominated in JET^[116-119] (higher / lower torus gas pressures respectively). For the present pairs of plasmas, density pedestals therefore emerge in proportion to their sources rather than their sizes, reminiscent of edge profile shaping as exemplified before on DIII-D^[3,20,28-30].

6. Summary and discussion

Effects influencing formation of the H-mode density pedestal have been investigated by comparing plasmas with identical values of edge dimensionless variables v_{*e}^{ped} , ρ_*^{ped} , β^{ped} , q_{95} in a common single-null divertor geometry on the Alcator C-Mod and JET tokamaks. Correspondence of these quantities ensures local plasma transport should be exactly the same^[42-45], while susceptibility to other factors not a priori following the same scaling, such as edge sources, is very stringently tested by the large ratio in absolute size, >4 , between these devices plus their pronounced contrast in recycling behaviour. At the requisite fields, currents and powers (7.9 T, 1.3 MA, $P_{\text{RF}} = 3.0$ MW on C-Mod, 1.4 T, 0.91 MA, $P_{\text{RF}} = 3.0$ MW on JET), respectively near the upper and lower operational limits of each machine, somewhat different H-regimes were obtained. On C-Mod, conventional ELM-free

states with rising density and radiation prevailed, reminiscent of earlier high-field studies^[60,61]. On the other hand, for JET very steady plasmas despite only minor, irregular ELMs emerged, possibly related to a large radiated power fraction within the confined volume. This allowed rather different scaled properties to develop in the cores of counterpart pulses in either machine, departing from the usual H-mode observation that pedestal values constitute a strong boundary condition for the core^[5-11]. Nevertheless, scaled efflux powers through their peripheries remained closely equal, while JET cases were demonstrated to be only marginally removed from conventional ELM-free behaviour. Hence their edge profiles could still be informatively compared.

Pedestal details were detected on C-Mod with a millimetre-resolution edge Thomson scattering diagnostic^[4,10,72,73] and on JET with a new high-resolution (HRTS) system^[52,53] which offers measurements below the ranges of its previous instrumentation^[54,55]. Interpolating these data using an established hyperbolic tangent parameterisation^[4,10,33,64] showed that, apart perhaps from unresolved Z_{eff} figures, plasmas were non-dimensionally matched at the pedestal tops for the highest C-Mod densities obtained. Accompanying widths for the electron temperature pedestal Δ_{T_e} were less definitely determined on JET, since only a single datapoint tended to fall in their steep gradient zones. Hence $\Delta_{T_e}^{\text{JET}}$ was likely to have lain between the scaled C-Mod value and a somewhat broader interpolated shape. However, density pedestal widths $\Delta_{n_e}^{\text{JET}}$ were more reliably defined, and were systematically greater than for C-Mod in proportion to machine size, ie $\Delta_{n_e}^{\text{JET}} / a_{\text{JET}} > \Delta_{n_e}^{\text{C-Mod}} / a_{\text{C-Mod}}$. Interestingly this implies the density pedestal was comparable to or larger in thickness than the temperature on JET, opposite to the general trend on C-Mod^[4,10,33]. More particularly, though, the clear departure from linear scaling between devices, even when the pedestal tops were non-dimensionally identical, revealed other factors apart from plasma transport must have been affecting the edge density profile in at least one of the two tokamaks. Estimates of neutral-particle sources were derived with the 1-D kinetic code^[56] KN1D for C-Mod and JET, corroborated for the latter also by separate fluid-plasma / kinetic-gas transport modelling with the 2-D EDGE2D-NIMBUS code suite^[57,58]. Superimposition of these respective normalised ionisation distributions against a coordinate normalised by density pedestal widths disclosed their closely equivalent decay-lengths, strongly suggesting Δ_{n_e} was correlated with this fall-off distance. Consequently, for the collisional, low-normalised-pressure plasma edges at $q_{95} \approx 4.2$ investigated, thickness of the density pedestal appeared to be expanded on JET by more deeply penetrating particle sources, and could similarly have been at least partly influenced by counterpart ionisation on C-Mod.

This finding tends to accord with the simplest picture of edge density profile formation, based upon local particle balance, embodied in the Engelhardt-Wagner-Lackner-Mahdavi^[16-20] description and previously recognised especially on DIII-D^[3,20,28-30]. It is also in agreement with an earlier edge-identity trial between DIII-D and JET^[23]. However, it stands in contrast to some other pedestal studies, such as on ASDEX Upgrade for which clear dominance of plasma transport in both electron temperature and density properties was concluded^[32]. Most notably, it differs from another identity comparison between C-Mod and DIII-D^[50], where both time-averaged T_e and n_e scaled profiles did coincide across the entire pedestal when non-dimensionally matched at their tops, ie their widths Δ did scale linearly with machine size. Consideration of time-averaged quantities in the latter and present investigations reduces the probability that such distinct behaviour might be due to random fluctuations of edge shapes. An alternative explanation could therefore be that the diversity of pedestal width

dependencies seen is related to the specific ranges of dimensionless, or indeed dimensional, plasma variables (and possibly magnetic configurations) realised in each set of experiments. In other words, different regimes of width variation might tend to occur in different regions of dimensionless parameter space, or for different absolute levels of density, power etc. This hypothesis is a subject for further work, but important connotations arise from the contrasting results encountered in any case. For a global quantity like the product of ion cyclotron frequency and energy confinement time $\omega_{ci} \tau_E$, it is well established^[120 - 125] that its scaling conforms with the dependence on v_{*e} , ρ_* , β , q_{95} , plus other equilibrium terms first elaborated by Kadomtsev^[42], perhaps adding in extra factors like proximity to the Greewald limit and central peaking^[126]. The dimensionless scaling is even preserved if $\omega_{ci} \tau_E$ is separated into core and pedestal components^[127]. A crucial consequence of such Kadomtsev-like behaviour is that variations with individual dimensionless arguments can be unambiguously tested in similarity scans where all the others are held constant as just the one in question is incremented^[128]. For density pedestal widths as obtained in the present C-Mod and JET identity plasmas, though, their combined sensitivity to particle sources, which are outside the scope of the non-dimensional relations^[44,45], means they do not comply with the same type of adjustment. On the contrary, their non-Kadomtsev-like scaling would imply an attempted similarity scan beginning from such a point would not be able to distinguish whether any changes observed in Δ_{n_e} were due to the step in chosen dimensionless variable or to consequential ones in edge sources. Before any pedestal width scaling with ρ_* , v_{*e} or β can be examined, therefore, it becomes necessary to determine that the conditions sought remain within a Kadomtsev-like domain, and in particular that they do not extend outside it as in these latest C-Mod and JET cases.

The authors gratefully acknowledge the support of Prof Y Kamada for these experiments under the ITPA Pedestal Group. This work was partly conducted under the European Fusion Development Agreement and was partly supported by the UK Engineering and Physical Sciences Research Council and by the European Communities under the contract of Association between EURATOM and UKAEA. The views and opinions expressed herein do not necessarily reflect those of the European Commission. Studies on Alcator C-Mod were supported by US Department of Energy award DE-FC02-99ER54512.

References

1. M Shimada *et al* Nucl. Fusion **47** (2007) S1
2. A E Hubbard Plasma Phys. Control. Fusion **42** (2000) A15
3. R J Groebner *et al* Fusion Sci. and Technol. **48** (2005) 1011
4. J W Hughes *et al* Fusion Sci. and Technol. **51** (2007) 317
5. G R Saibene *et al* Nucl. Fusion **39** (1999) 1133
6. R Sartori *et al* Proc. 20th IAEA Fusion Energy Conference, Vilamoura, Nov. 2004, IAEA-CN-116-EX/6-3 (IAEA, Vienna, 2005),
http://www-naweb.iaea.org/naweb/physics/fec/fec2004/papers/ex_6-3.pdf
7. P Monier-Garbet *et al* Nucl. Fusion **45** (2005) 1404
8. W Suttrop *et al* Plasma Phys. Control. Fusion **42** (2000) A97
9. G Tardini *et al* Nucl. Fusion **42** (2002) 258
10. J W Hughes *et al* Phys. Plasmas **9** (2002) 3019
11. C F Maggi *et al* Nucl. Fusion **47** (2007) 535
12. M Valovič *et al* 11th IAEA Technical Meeting on H-mode Physics and Transport Barriers, Tsukuba, Sept. 2007, J. Phys. Conf. Series **123** (2008) 012039
13. H Y Guo *et al* Nucl. Fusion **40** (2000) 69
14. M F F Nave *et al* Plasma Phys. Control. Fusion **42** (2000) A89
15. R J Groebner & T H Osborne
Phys. Plasmas **5** (1998) 1800
16. F Wagner & K Lackner in “Physics of plasma-wall interactions in controlled fusion”, NATO ASI Series B: Physics vol. **131** (Plenum Press, New York, 1986), eds. D E Post & R Behrisch, p. 931
17. W Engelhardt & W Feneberg
J Nucl. Mat. **76&77** (1978) 518
18. W Engelhardt *et al* J Nucl. Mat. **111&112** (1982) 337
19. M A Mahdavi *et al* Nucl. Fusion **42** (2002) 52
20. M A Mahdavi *et al* Phys. Plasmas **10** (2003) 3984
21. F L Hinton & G M Staebler
Phys. Fluids B **5** (1993) 1281
22. P C Stangeby J. Phys. D: Appl. Phys. **36** (2003) 2784
23. M E Fenstermacher *et al* Nucl. Fusion **45** (2005) 1493
24. C L Rettig *et al* Nucl. Fusion **33** (1993) 643
25. T Fukuda *et al* Plasma Phys. Control. Fusion **36** (1994) A87
26. F Ryter *et al* Plasma Phys. Control. Fusion **40** (1998) 725
27. G P Maddison *et al* Proc. 32nd EPS Conference on Plasma Phys., Tarragona, June 2005, ECA Vol.**29C**, P-4.043 (2005),
http://eps2005.ciemat.es/papers/pdf/P4_043.pdf

28. R J Groebner *et al* Plasma Phys. Control. Fusion **44** (2002) A265
29. R J Groebner *et al* Phys. Plasmas **9** (2002) 2134
30. R J Groebner *et al* Nucl. Fusion **44** (2004) 204
31. A Kirk *et al* Plasma Phys. Control. Fusion **46** (2004) A187
32. I Nunes *et al* Nucl. Fusion **45** (2005) 1550
33. J W Hughes *et al* Phys. Plasmas **13** (2006) 056103
34. J W Hughes *et al* Nucl. Fusion **47** (2007) 1057
35. J W Connor Plasma Phys. Control. Fusion **40** (1998) 531
36. J W Connor *et al* Phys. Plasmas **5** (1998) 2687
37. H R Wilson *et al* Phys. Plasmas **6** (1999) 1925
38. P B Snyder & H R Wilson Plasma Phys. Control. Fusion **45** (2003) 1671
39. D A Mossessian *et al* Plasma Phys. Control. Fusion **44** (2002) 423
40. T H Osborne *et al* Plasma Phys. Control. Fusion **40** (1998) 845
41. T H Osborne *et al* J Nucl. Mat. **266-269** (1999) 131
42. B B Kadomtsev Sov. J. Plasma Phys. **1** (1975) 295
43. J W Connor & J B Taylor Nucl. Fusion **17** (1977) 1047
44. K Lackner Comments Plasma Phys. Controlled Fusion **13** (1990) 163
45. K Lackner Comments Plasma Phys. Controlled Fusion **15** (1994) 359
46. M Greenwald *et al* Nucl. Fusion **28** (1988) 2199
47. F Ryter *et al* Plasma Phys. Control. Fusion **44** (2002) A415
48. J A Snipes *et al* Proc. 19th IAEA Fusion Energy Conference, Lyon, Oct. 2002, IAEA-CN-94-CT/P-04 (IAEA, Vienna, 2003),
http://www.iaea.org/programmes/ripc/physics/fec2002/pdf/ctp_04.pdf
49. W Suttrop *et al* *ibid*, IAEA-CN-94-EX/P5-07 (IAEA, Vienna, 2003),
http://www.iaea.org/programmes/ripc/physics/fec2002/pdf/exp5_07.pdf
50. D A Mossessian *et al* Phys. Plasmas **10** (2003) 689
51. G R Saibene *et al* Plasma Phys. Control. Fusion **46** (2004) A195
52. R Pasqualotto *et al* Rev. Sci. Instrum. **75** (2004) 3891
53. R Pasqualotto *et al* Proc. 12th Int. Symposium on laser-aided plasma diagnostics, Snowbird, Sept. 2005, p. 324 (CD-ROM)
54. D A Mossessian *et al* Proc. 30th EPS Conference on Contr. Fusion and Plasma Phys., St. Petersburg, July 2003, ECA Vol.27A, P-3.182 (2003),
http://epsppd.epfl.ch/StPetersburg/PDF/P3_182.PDF
55. G P Maddison *et al* *ibid*, P-1.109 (2003),
http://epsppd.epfl.ch/StPetersburg/PDF/P1_109.PDF
56. B LaBombard MIT PSFC report RR-01-3, Aug. 2001, *see*
http://www.psfc.mit.edu/~labombard/KN1D_Source_Info.html
57. A Taroni *et al* Contrib. Plasma Phys. **32** (1992) 438
58. R Simonini *et al* Contrib. Plasma Phys. **34** (1994) 368

59. O Sauter, C Angioni & Y R Lin-Liu
Phys. Plasmas **6** (1999) 2834
60. Y Takase *et al*
Phys. Plasmas **4** (1997) 1647
61. A E Hubbard *et al*
Phys. Plasmas **14** (2007) 056109
62. K Borrass
Nucl. Fusion **42** (2002) 1251
63. M Greenwald *et al*
Phys. Plasmas **6** (1999) 1943
64. A E Hubbard *et al*
Phys. Plasmas **8** (2001) 2033
65. A E Hubbard *et al*
Plasma Phys. Control. Fusion **48** (2006) A121
66. J Stober *et al*
Nucl. Fusion **41** (2001) 1123
67. M Bécoulet *et al*
Plasma Phys. Control. Fusion **45** (2003) A93
68. A Loarte *et al*
Phys. Plasmas **11** (2004) 2668
69. G R Saibene *et al*
Nucl. Fusion **45** (2005) 297
70. F Troyon *et al*
Plasma Phys. Control. Fusion **26** (1984) 209
71. D A Mossessian, A E Hubbard & J Irby
Rev. Sci. Instrum. **70** (1999) 759
72. J W Hughes *et al*
Rev. Sci. Instrum. **72** (2001) 1107
73. J W Hughes *et al*
Rev. Sci. Instrum. **74** (2003) 1667
74. H Salzmann *et al*
Rev. Sci. Instrum. **59** (1988) 1451
75. C W Gowers *et al*
Rev. Sci. Instrum. **66** (1995) 471
76. O J W F Kardaun *et al*
Proc. "Theory of Fusion Plasmas" Workshop, Varenna, Aug. 1987 (Editrice Compositori, Bologna, 1988), eds. A Bondeson, E Sindoni & F Troyon, p.435
77. G Becker
Nucl. Fusion **32** (1992) 1064
78. X Garbet *et al*
Plasma Phys. Control. Fusion **46** (2004) 1351
79. X Garbet *et al*
Plasma Phys. Control. Fusion **47** (2005) 957
80. P Mantica *et al*
Proc. 20th IAEA Fusion Energy Conference, Vilamoura, Nov. 2004, EX/P6-18 (IAEA, Vienna, 2005),
http://www-naweb.iaea.org/napc/physics/fec/fec2004/papers/ex_p6-18.pdf
81. P Mantica & F Ryter
Comptes Rendus Physique **7**, #6 (2006) 634
82. J A Snipes *et al*
Plasma Phys. Control. Fusion **43** (2001) L23
83. A Mazurenko *et al*
Phys. Rev. Lett. **89** (2002) 225004
84. J A Snipes *et al*
Proc. 29th EPS Conference on Plasma Phys. and Contr. Fusion, Montreux, June 2002, ECA Vol. **26B**, P-1.057 (2002),
http://epsppd.epfl.ch/Montreux/pdf/P1_057.pdf
85. D A Mossessian *et al*
Phys. Plasmas **10** (2003) 1720
86. A Loarte *et al*
Plasma Phys. Control. Fusion **44** (2002) 1815
87. A B Mikhailovskii
"Instabilities in a confined plasma", (IoP Publishing, Bristol, 1998), p.415
88. C Z Cheng & M S Chance
Phys. Fluids **29** (1986) 3695

89. B N Breizmann & S E Sharapov
Plasma Phys. Control. Fusion **37** (1995) 1057
90. G Y Fu
Phys. Plasmas **2** (1995) 1029
91. P Smeulders *et al*
Plasma Phys. Control. Fusion **41** (1999) 1303
92. C P Perez *et al*
Plasma Phys. Control. Fusion **46** (2004) 61
93. R Betti & J P Freidberg
Phys. Fluids B **4** (1992) 1465
94. S Hacquin *et al*
Nucl. Fusion **46** (2006) S714
95. G P Maddison *et al*
Plasma Phys. Control. Fusion **44** (2002) 1937
96. A Loarte *et al*
Plasma Phys. Control. Fusion **45** (2003) 1549
97. R Behn *et al*
Plasma Phys. Control. Fusion **49** (2007) 1289
98. R J Groebner & T N Carlstrom
Plasma Phys. Control. Fusion **40** (1998) 673
99. R J Groebner *et al*
Nucl. Fusion **41** (2001) 1789
100. A Kallenbach *et al*
Plasma Phys. Control. Fusion **46** (2004) 431
101. S I Braginskii
Reviews of Plasma Physics, vol. **1** (Consultants Bureau, New York, 1965), ed M A Leontovich, p. 205
102. G J Radford *et al*
Contrib. Plasma Phys. **36** (1996) 187
103. A V Chankin
J Nucl. Mat. **241-243** (1997) 199
104. A V Chankin *et al*
J Nucl. Mat. **290-293** (2001) 518
105. W Eckstein
“Computer simulation of ion-solid interaction”, Springer Series in Materials Science, vol. **10** (Springer-Verlag, Berlin, 1991)
106. B Lehnert
Nucl. Fusion **8** (1968) 173
107. B Lehnert
Nucl. Fusion **23** (1983) 1327
108. R K Janev *et al*
“Elementary processes in hydrogen-helium plasmas: cross-sections and reaction rate coefficients”, Springer Series on Atoms and Plasmas, vol. **4** (Springer-Verlag, Berlin, 1987)
109. R S Freund *et al*
J. Chem. Phys. **64** (1976) 1122
110. D H McNeill *et al*
J. Vac. Sci. Technol. A **2** (1984) 689
111. L C Johnson & E Hinnov
J. Quant. Spectrosc. Radiat. Transfer **13** (1973) 333
112. R L Boivin *et al*
Phys. Plasmas **7** (2000) 1919
113. B LaBombard *et al*
Nucl. Fusion **40** (2000) 2041
114. B LaBombard *et al*
Phys. Plasmas **8** (2001) 2107
115. B Lipschultz *et al*
Plasma Phys. Control. Fusion **44** (2002) 733
116. G R Saibene *et al*
J Nucl. Mat. **241-243** (1997) 476
117. L D Horton *et al*
Nucl. Fusion **39** (1999) 1
118. R D Monk *et al*
Nucl. Fusion **39** (1999) 1751
119. W Fundamenski
Fusion Sci. and Technol. **53** (2008) 1023
120. J P Christiansen *et al*
Nucl. Fusion **32** (1992) 291

- 121. J G Cordey *et al* Plasma Phys. Control. Fusion **39** (1997) B115
- 122. ITER Physics Expert Groups on Confinement and Transport & Confinement
Modelling and Database, ITER Physics Basis Editors
Nucl. Fusion **39** (1999) 2175
- 123. J G Cordey *et al* Nucl. Fusion **45** (2005) 1078
- 124. D C McDonald *et al* Nucl. Fusion **47** (2007) 147
- 125. E J Doyle *et al* Nucl. Fusion **47** (2007) S18
- 126. J G Cordey *et al* Plasma Phys. Control. Fusion **44** (2002) 1929
- 127. J G Cordey *et al* Nucl. Fusion **43** (2003) 670
- 128. D C McDonald *et al* Fusion Sci. and Technol. **53** (2008) 891

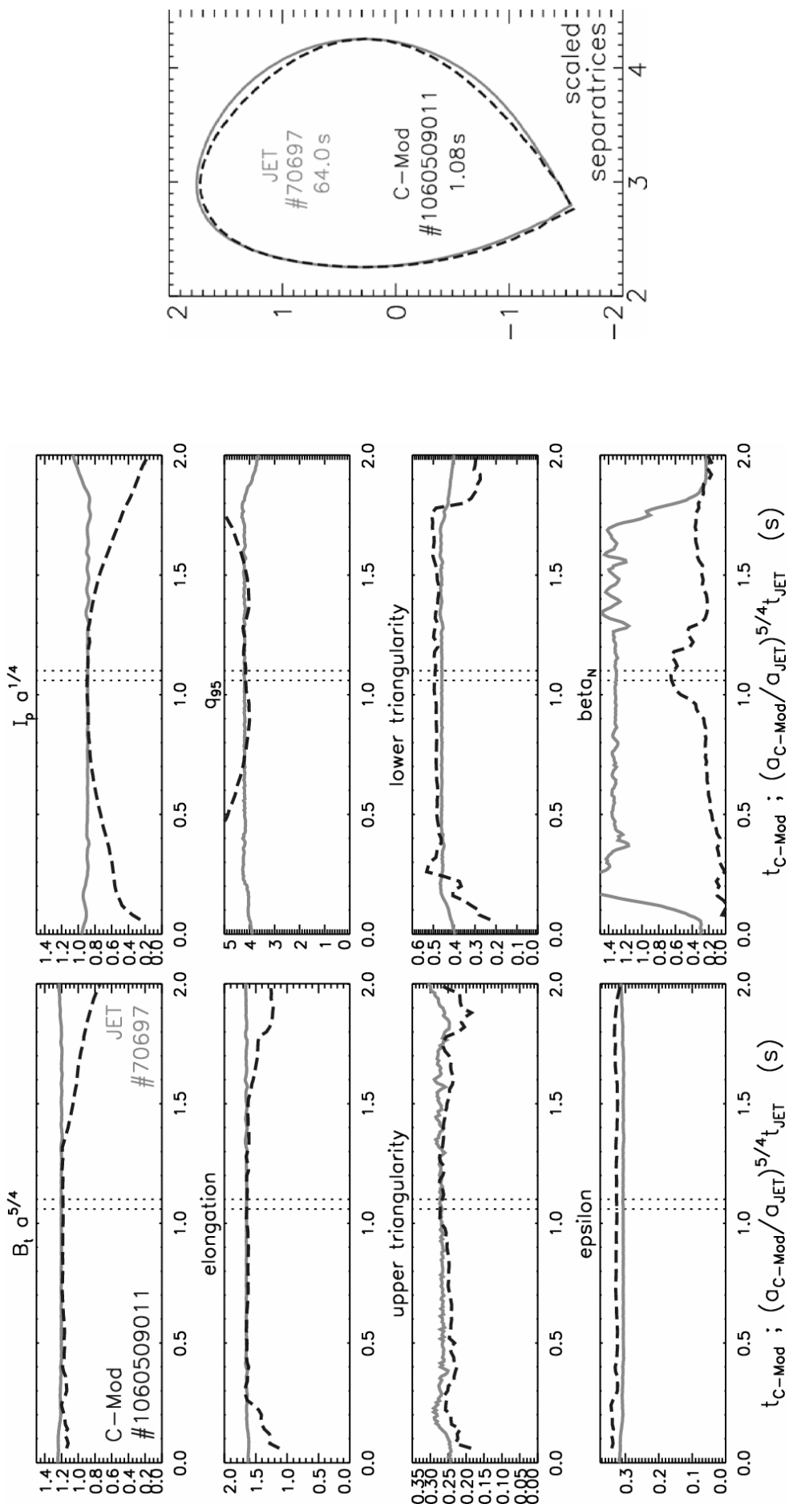


Fig.1 Scaled field and current, plus basic magnetic equilibrium parameters (elongation κ , edge safety factor q_{95} , upper triangularity δ^u , lower triangularity δ^l , inverse aspect ratio ϵ) and renormalised total pressure β_N from EFIT, for common single-null divertor configuration in C-Mod and JET. Time-scales of JET traces are scaled according to the ratio of minor radii, as explained in the text. Vertical dotted lines indicate the comparison interval. Inset: scaled separatrixes from EFIT at respective times corresponding to this period.

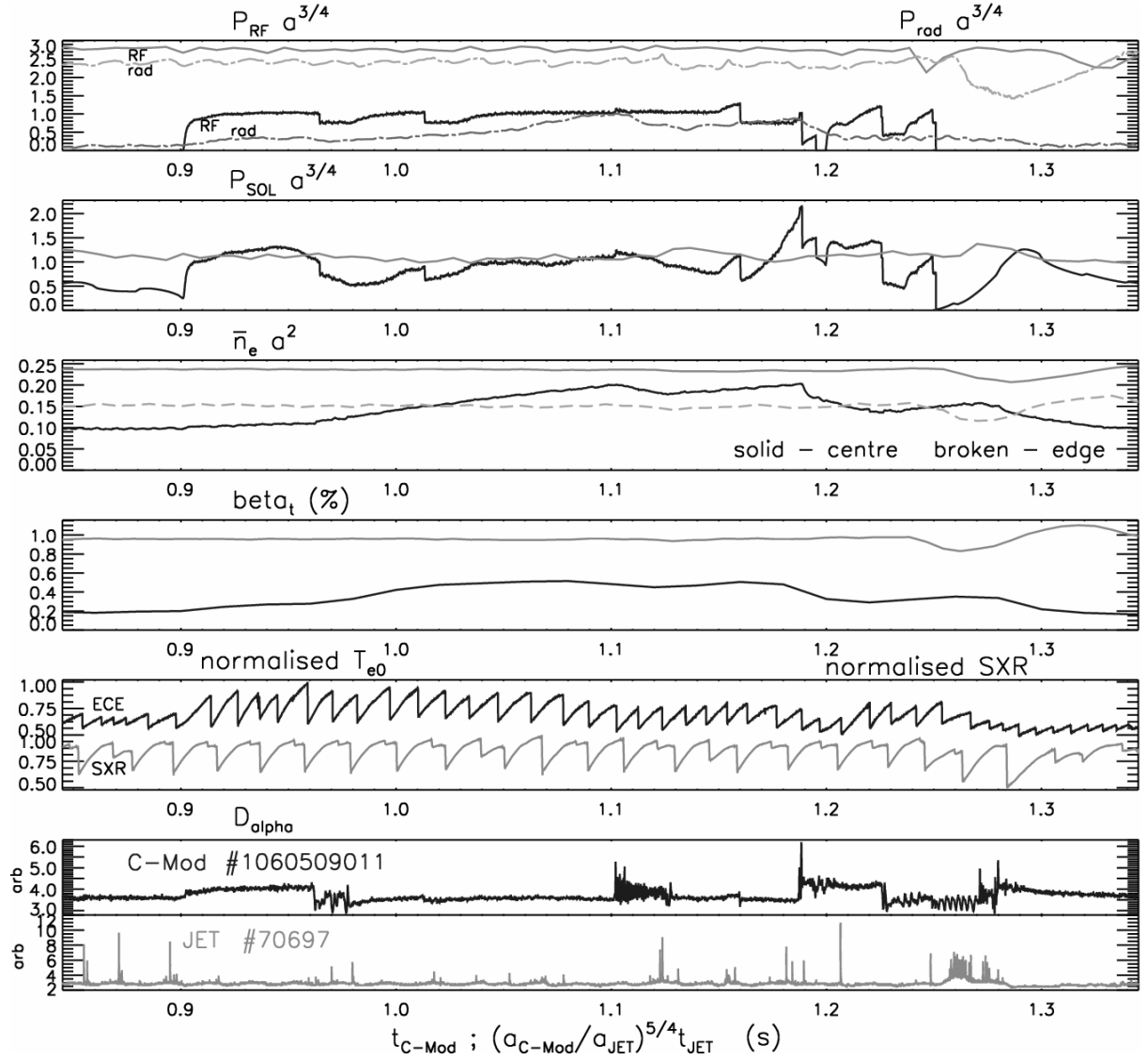


Fig.2 Summary properties of C-Mod and JET pulses, time-scales of JET quantities again scaled with ratio of minor radii: scaled ICRH and total radiated powers; scaled estimates of power efflux through the edge; scaled line-average electron density along a chord through the plasma centre (solid) and for JET also through the edge (broken); normalised total pressure β_t ; sawtooth oscillations indicated for C-Mod by normalised central electron temperature from ECE and for JET by normalised SXR emission along a central chord; line-integral $D\alpha$ emission.

greyscale in printed paper

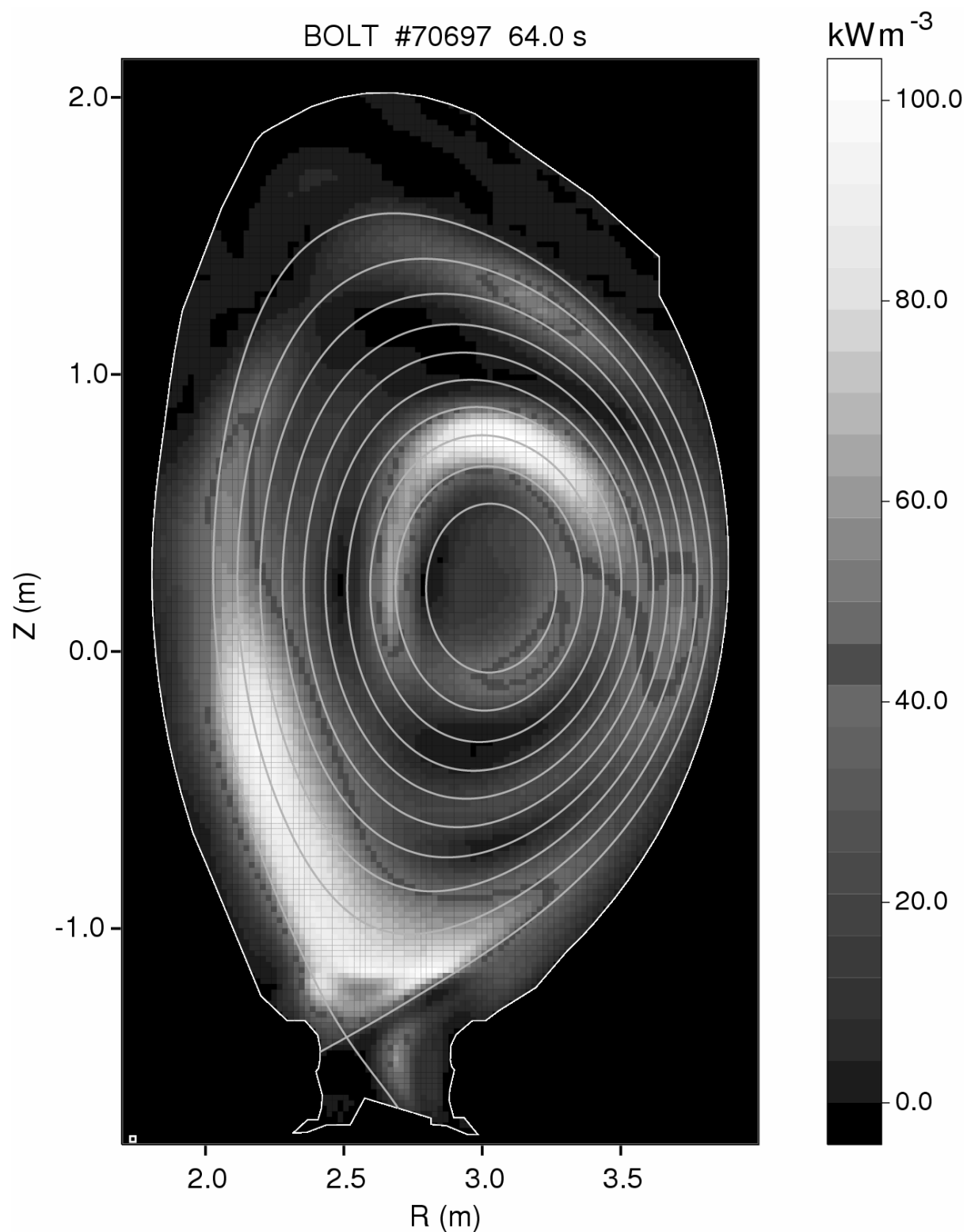


Fig.3 Tomographic reconstruction of total-radiation pattern from multiple bolometric lines-of-sight in JET pulse #70697 at the comparison time with C-Mod cases. Also superimposed: magnetic surfaces from EFIT and vessel first-wall contour, including the divertor at the bottom of the picture.

greyscale in printed paper

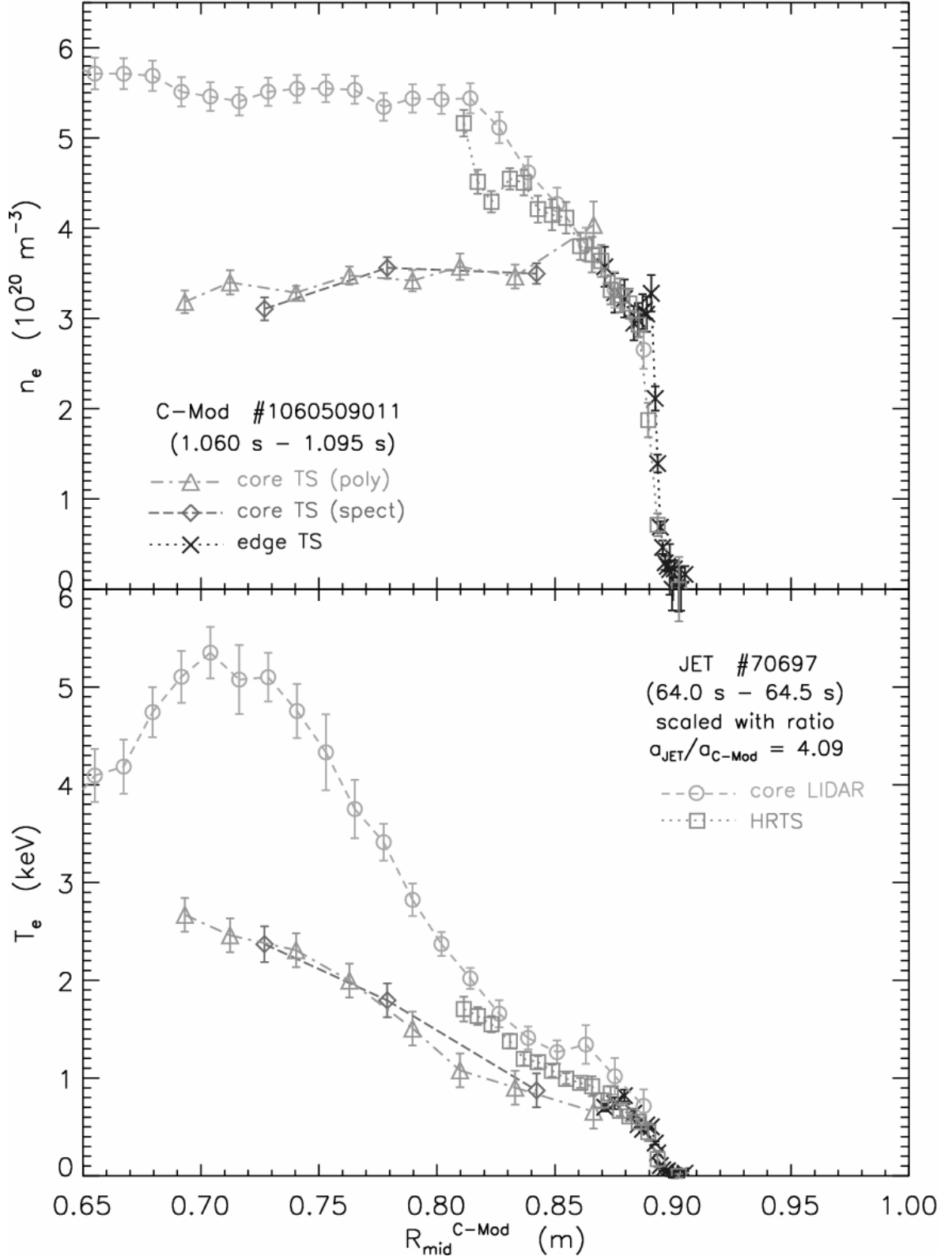


Fig.4 Profiles across the whole plasma minor radius for C-Mod and JET shot pair achieving closest dimensionless identity at the pedestal top, using a combination of Thomson-scattering diagnostics. JET data are time-averaged in the comparison interval, scaled with the ratio of minor radii and aligned on the separatrix from EFIT ($R_{\text{mid}}^{\text{C-Mod}} = 0.894 \text{ m}$).

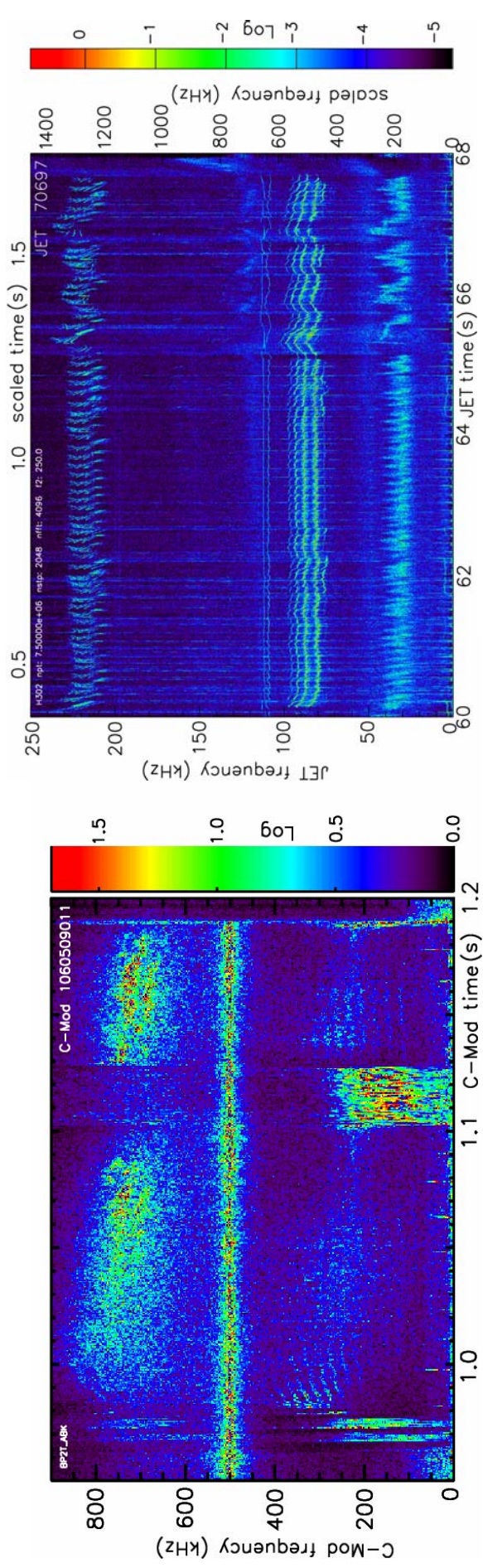


Fig.5 Power spectra of magnetic fluctuations over intervals spanning the comparison time for C-Mod (left) and JET (right) shots most closely fulfilling dimensionless identity at the pedestal top. Time and frequency axes scaled to C-Mod values according to equation (6) are also superimposed on the JET plot. Note logarithmic intensity ranges (in colour) differ for each machine.

colour in printed paper

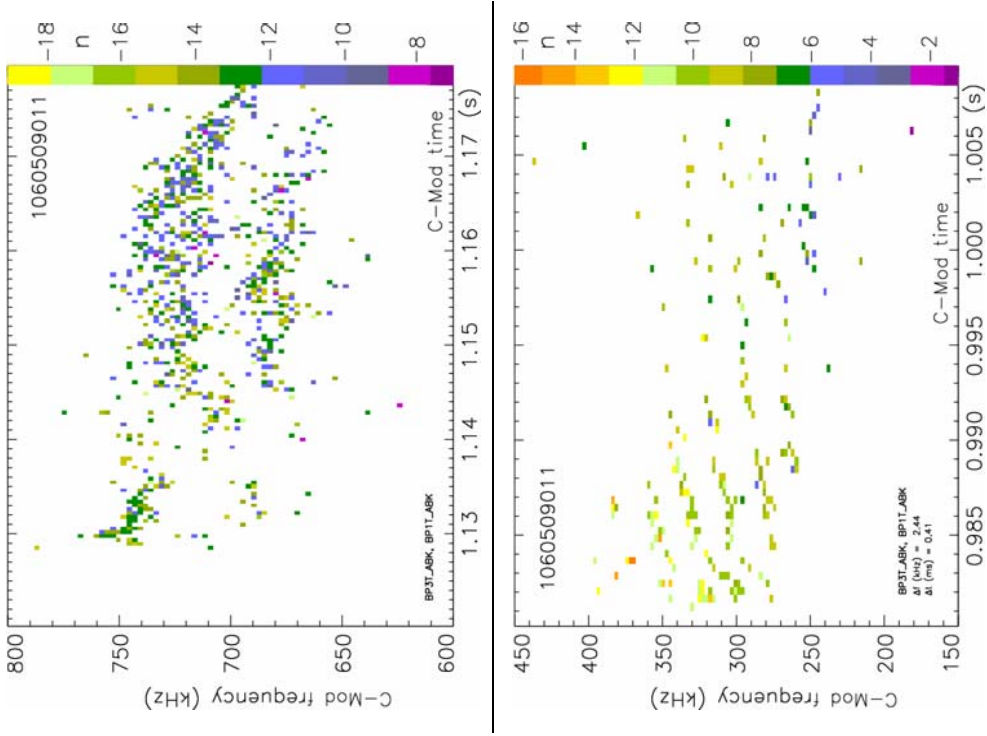


Fig.6 Estimated toroidal mode numbers from correlation of magnetic signals in the same C-Mod (left) and JET (right) plasmas. Scaled time and frequency axes are again added for the latter. Note different time intervals are plotted for lower and higher frequencies in C-Mod. Negative mode numbers signify rotation in the electron diamagnetic drift direction.

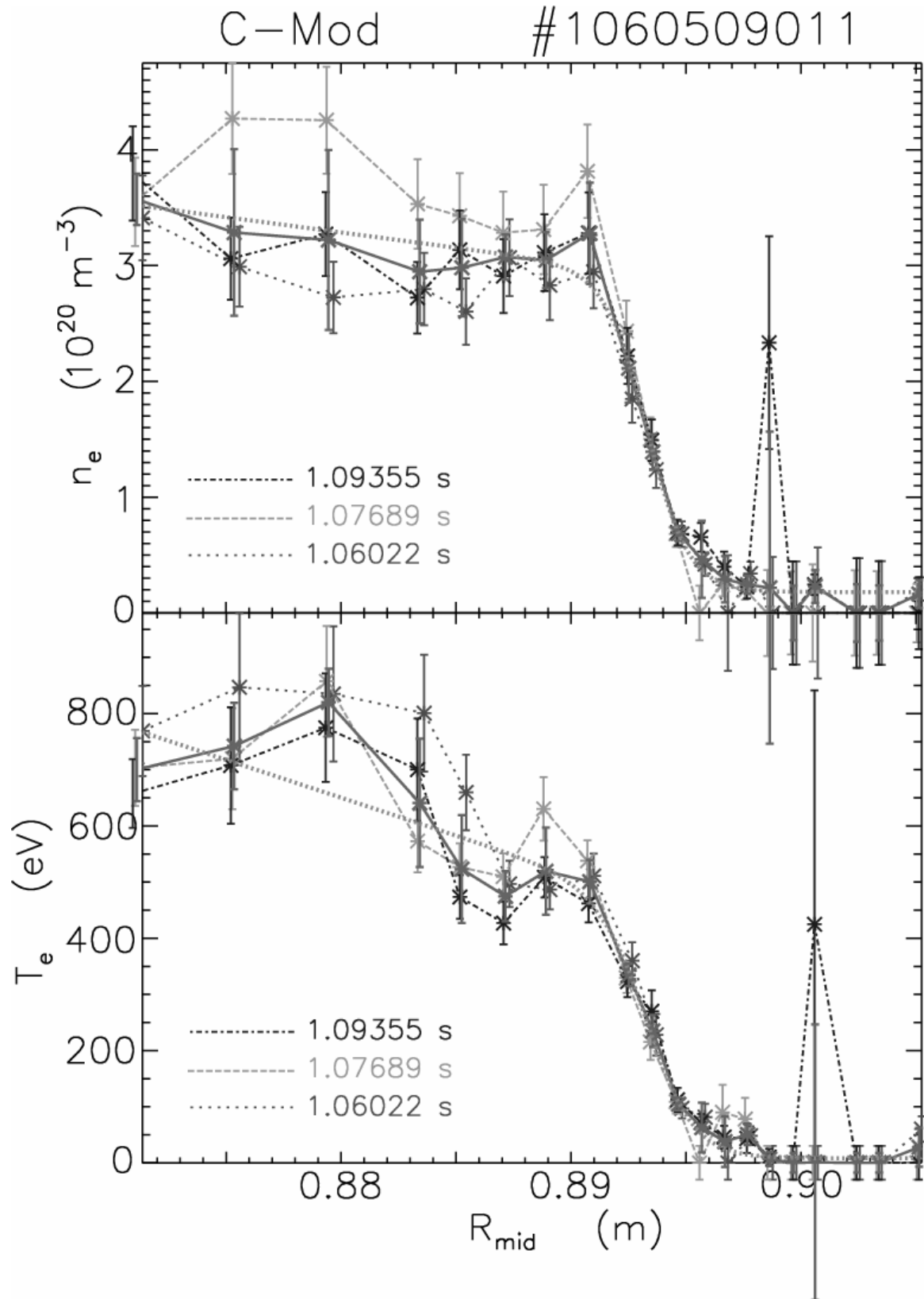


Fig.7 Example of 3 consecutive electron density and temperature profiles measured by edge Thomson scattering during ELM-free H-mode in C-Mod pulse #1060509011. Also superimposed: (solid line) error-weighted averages over these; (dotted line) modified tanh fits, as described in the text.

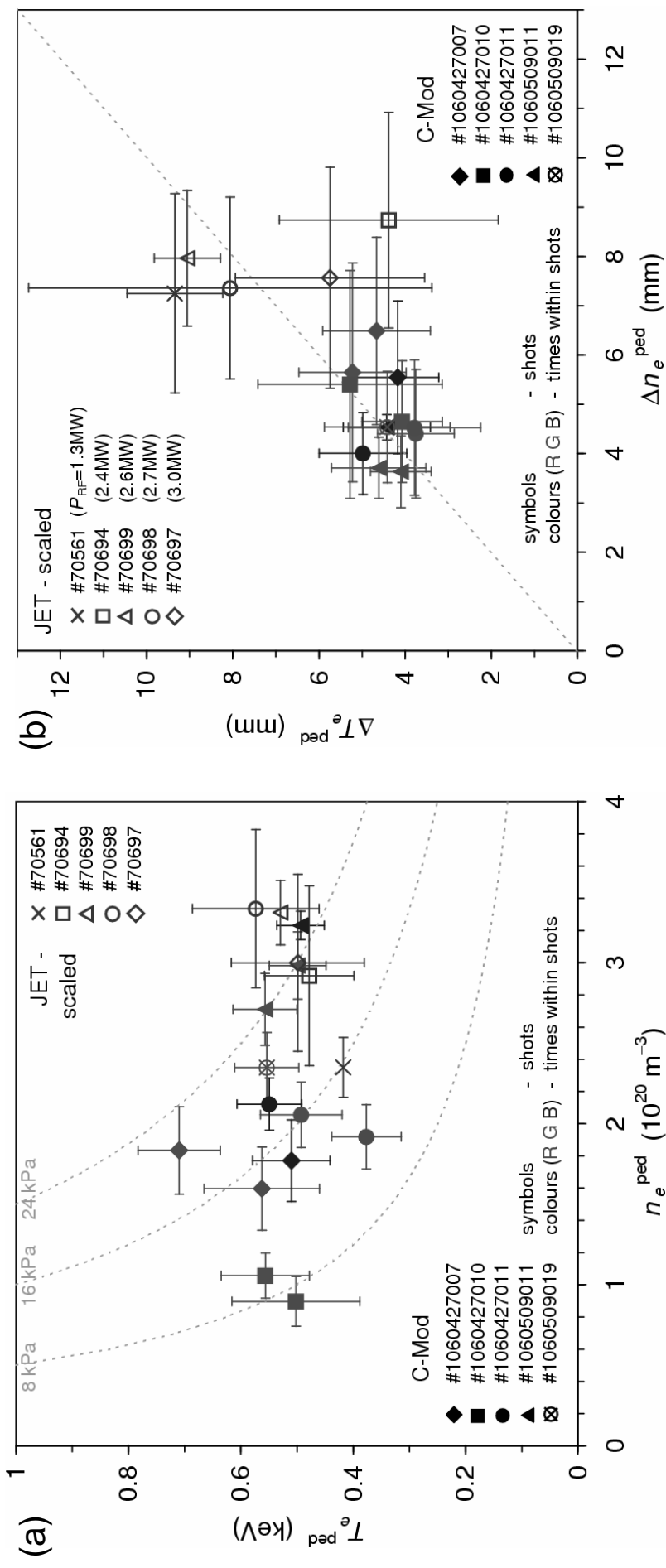


Fig.8 Electron density and temperature pedestal properties from modified tanh fits (equation (7) for C-Mod, (8) for JET) through scans in each device. C-Mod shots listed chronologically, time sequence within each one indicated in colour version of plots. JET shots in order of increasing P_{RF} . JET results are scaled to C-Mod ranges according to (4) for heights (a) and with size ratio for widths (b).

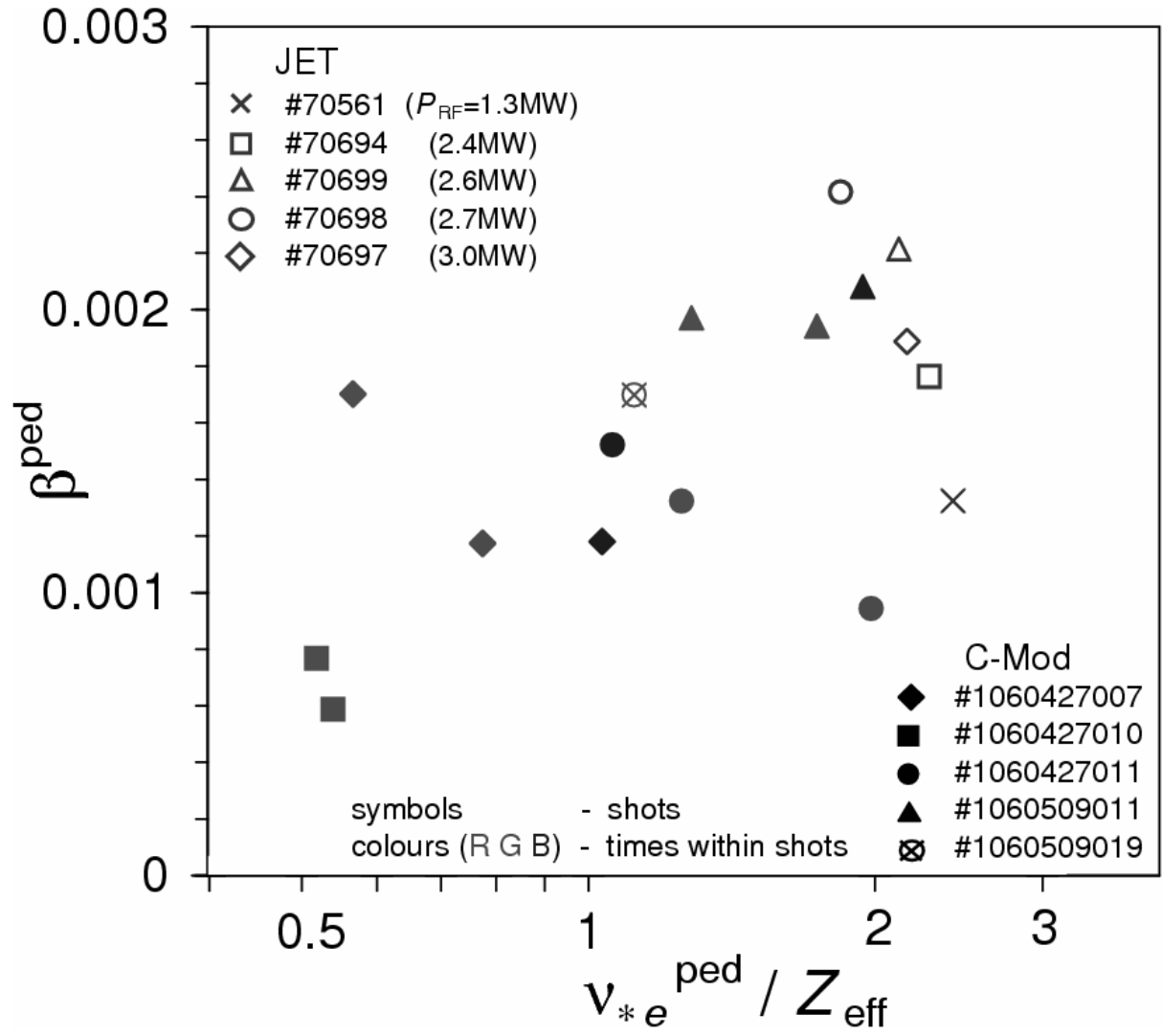


Fig.9 Estimates at the pedestal top of normalised pressure versus electron collisionality^[59] for a pure plasma, over the same sets of C-Mod and JET pulses as Fig.8. Time sequence within each C-Mod shot again depicted in colour version.

greyscale in printed paper

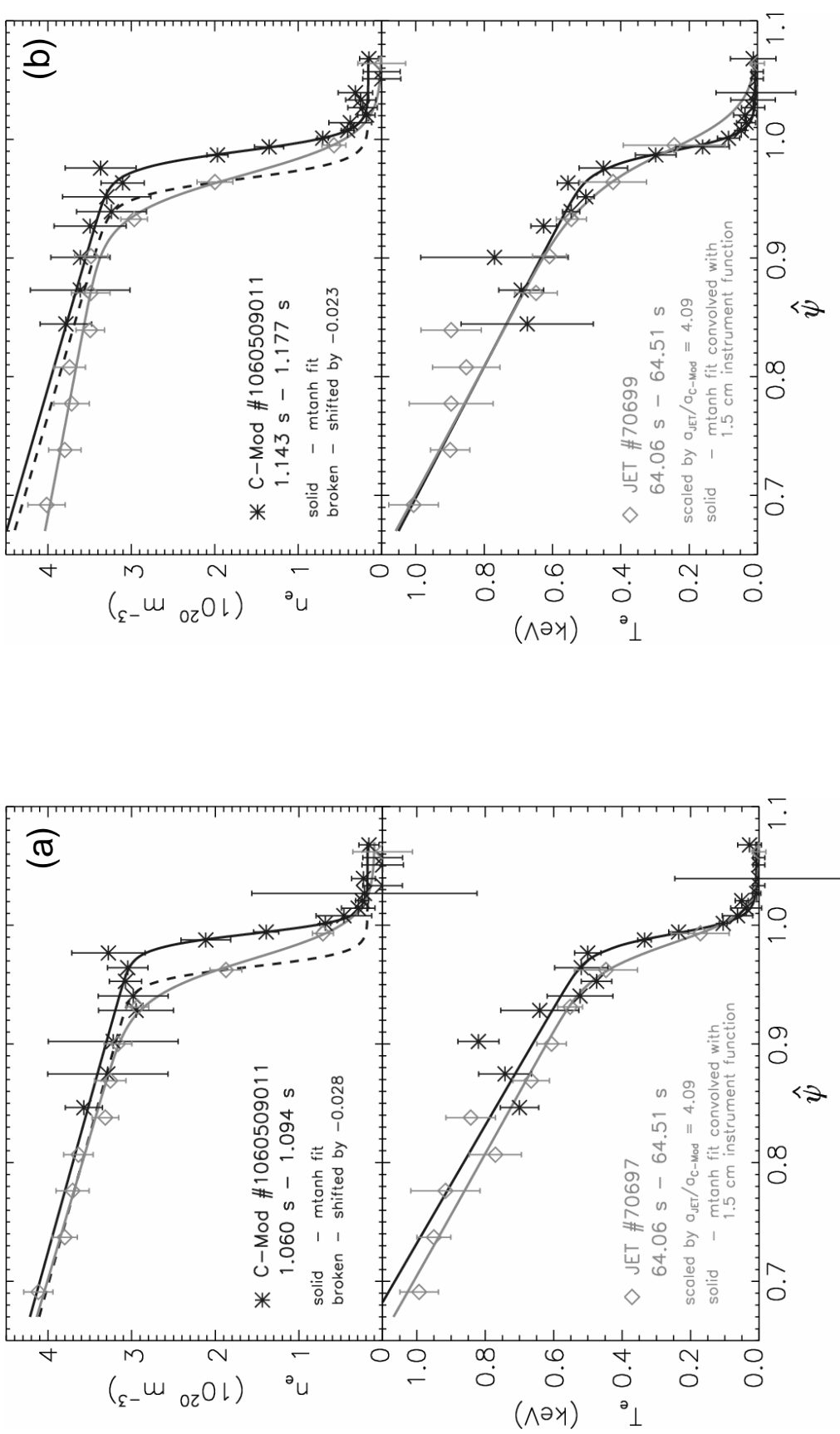


Fig.10 Overlay of C-Mod and JET averaged Thomson scattering profiles versus normalised poloidal flux, for the two shot pairs achieving closest non-dimensional matches at the pedestal top (viz in colour versions of Figs.8 & 9 respectively (a) filled green triangle and open diamond, (b) filled blue and open triangles). JET data are scaled onto C-Mod ranges according to (4). Modified tanh fits to C-Mod densities are also shifted (broken lines) for best alignment with JET counterparts, to emphasize their different gradients.

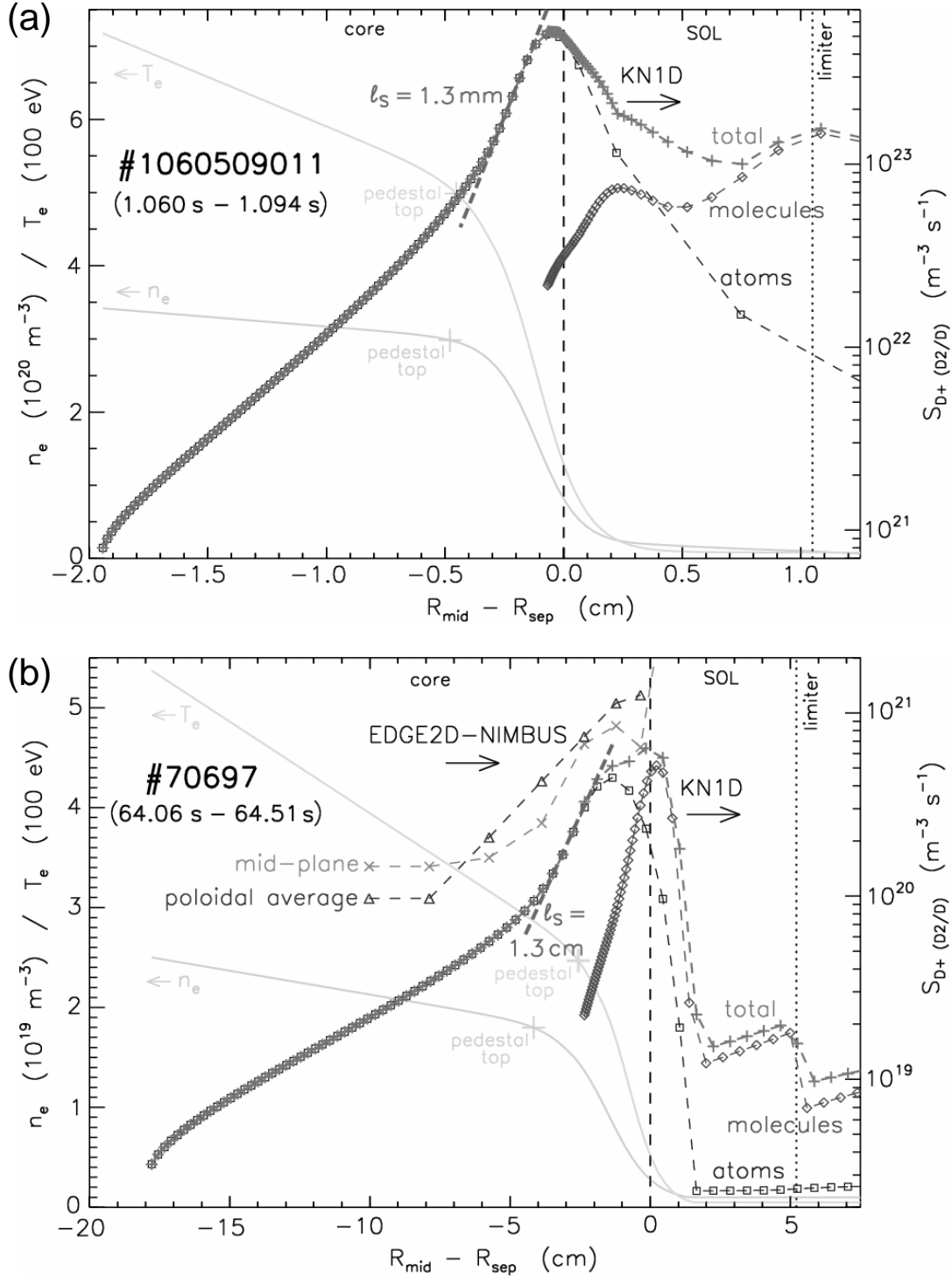


Fig.11 Edge ionisation source rates (right-hand scales) calculated with the 1-D KN1D^[56] code for (a) C-Mod and (b) JET shots with non-dimensionally identical pedestal tops. Components directly from molecular dissociative ionisations and from atoms, plus their sum, are shown. Source decay-lengths in the pedestal are indicated by heavy dashed lines. Respective plasma profiles (left-hand scales), on the same spatial coordinates centred on the separatrices, are shown as faint lines. Also superimposed for JET: source rates within the pedestal, at the mid-plane and poloidally-averaged around flux surfaces, computed with the 2-D EDGE2D-NIMBUS code suite^[57,58].

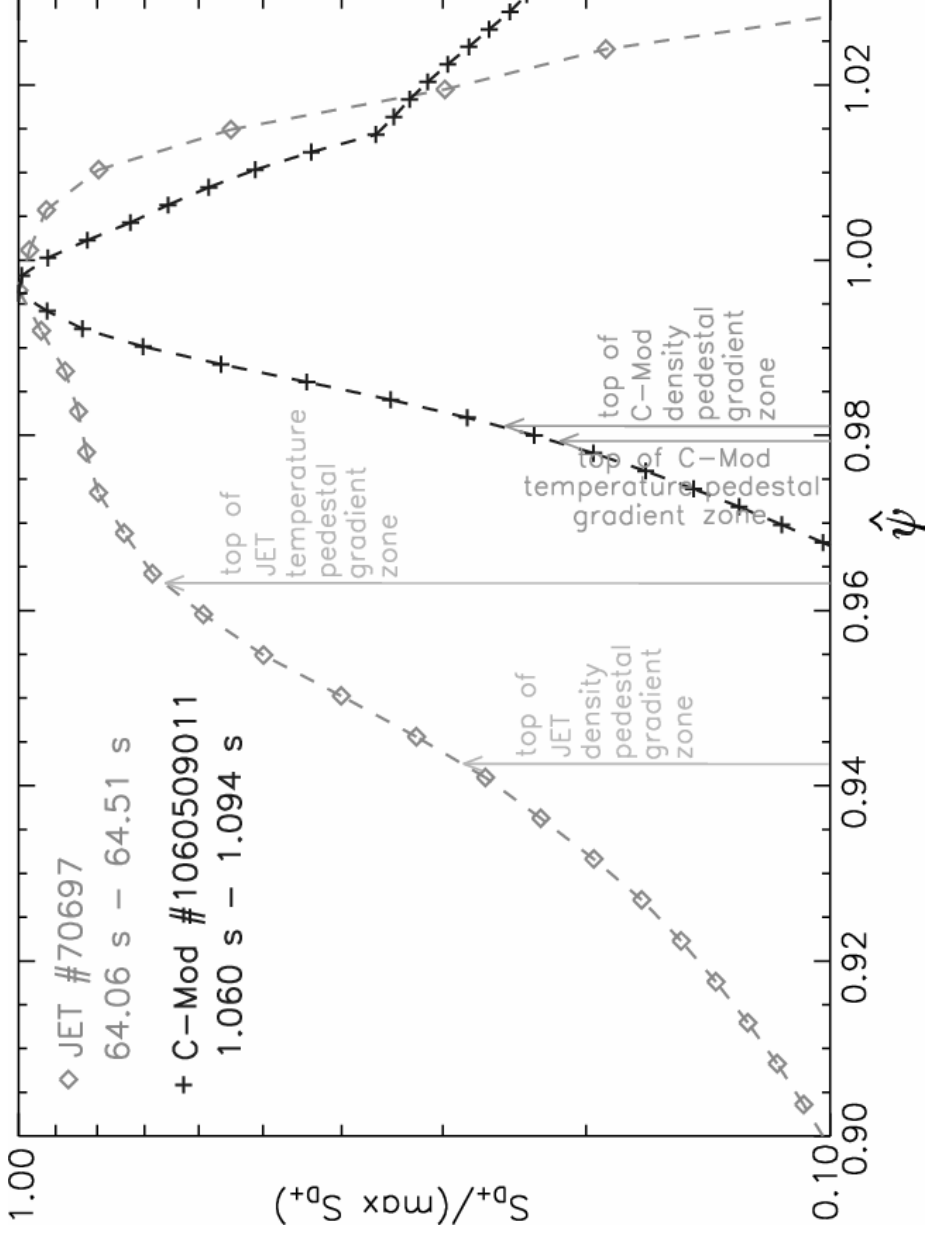


Fig.12 KN1D total ionisation rates from Fig.11 for a C-Mod and JET shot pair with closely identical pedestal tops, each normalised by its maximum value, and superimposed by plotting against normalised poloidal flux. Also indicated : positions interpolated onto this coordinate of the tops of the pedestal gradient regions for both density and temperature, defined as $R_c - d$ from the respective modified tanh fits used in the calculations.

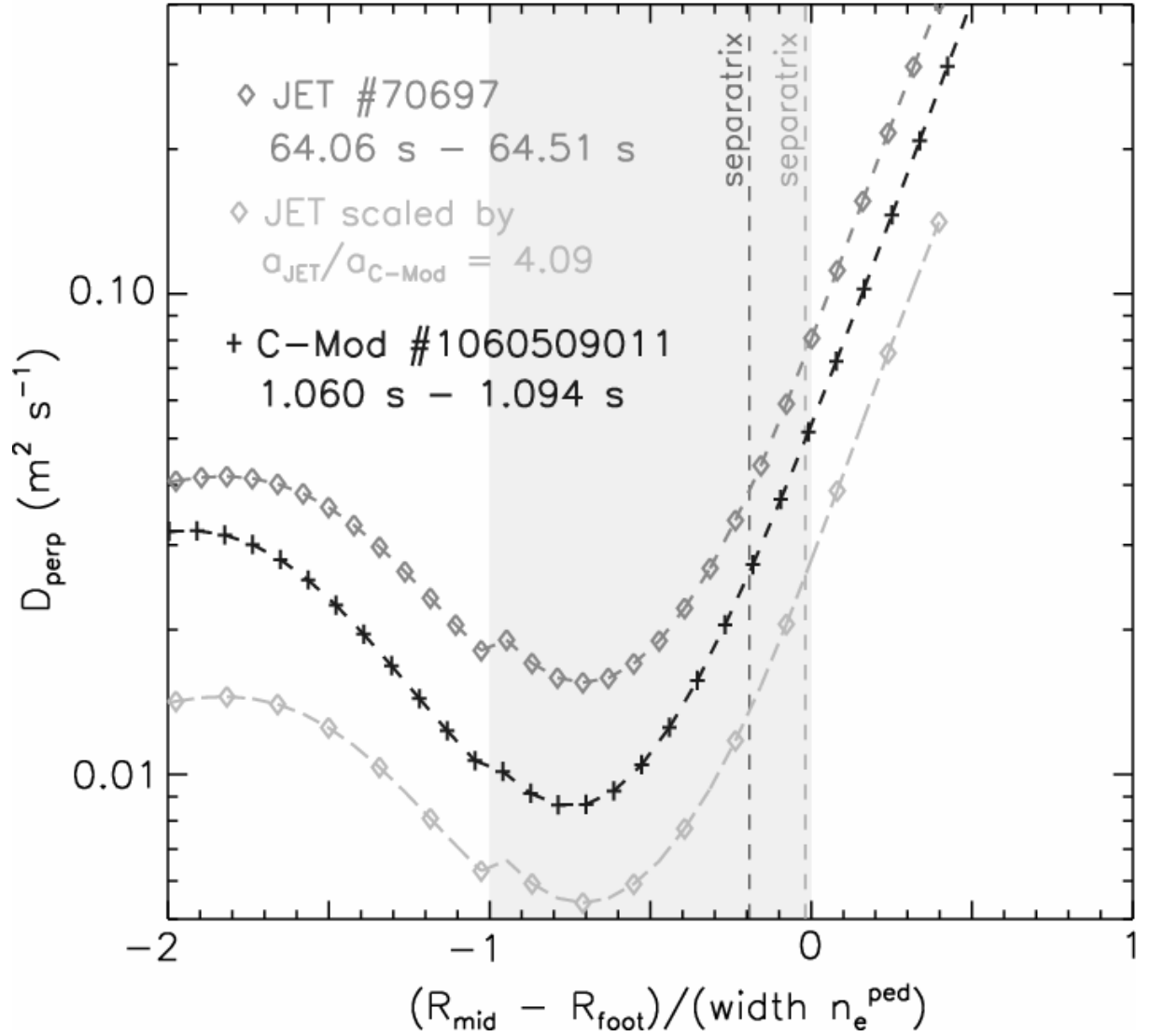


Fig.13 Estimated ion cross-field diffusivities from integration of the KN1D source rates in Fig.11. The abscissa is centred on the density-pedestal foot, defined as $R_{cn_e} + d_{n_e}$ in each device, and normalised by their respective widths $2d_{n_e}$. Thus the shaded region denotes the main gradient zone of the density pedestal. Separatrix positions versus this coordinate are indicated by vertical dashed lines. Also superimposed (lighter line): JET result scaled with the ratio of minor radii according to the dependence expected for coefficients following dimensionless identity ($D_{\perp} \sim a\sqrt{T_e} \sim a^{3/4}$).

greyscale in printed paper

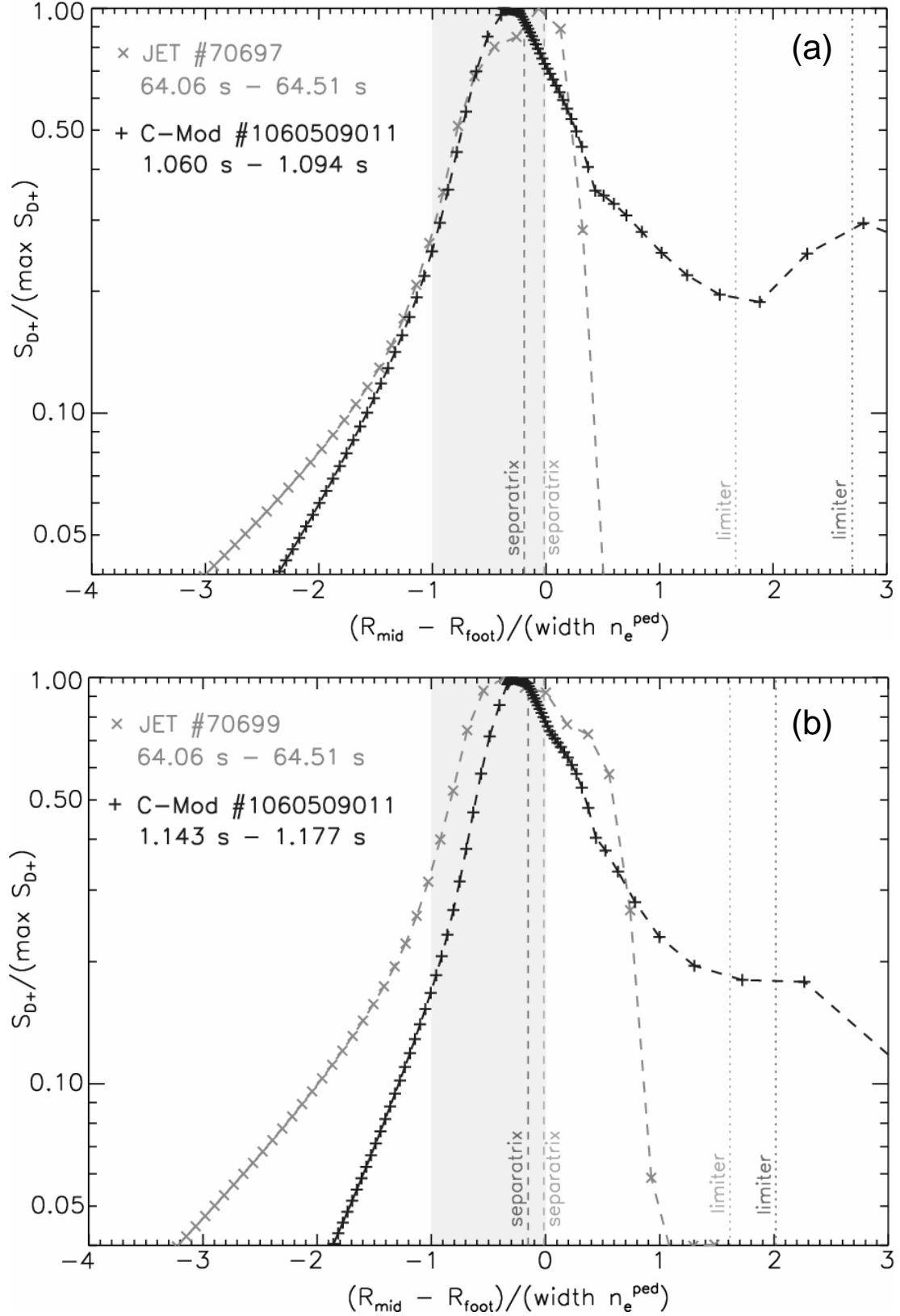


Fig.14 Normalised total ionisation sources from KN1D plotted against the normalised coordinate defined in Fig.13, for the two C-Mod and JET pedestal-top identity shot pairs depicted in Fig.10. Shaded regions again identify main gradient zones of the density pedestals.